HHS Public Access

Author manuscript

Nat Cell Biol. Author manuscript; available in PMC 2019 August 11.

Published in final edited form as:

Nat Cell Biol. 2019 March ; 21(3): 348–358. doi:10.1038/s41556-019-0272-y.

microRNA-dependent regulation of biomechanical genes establishes tissue stiffness homeostasis

Albertomaria Moro[1,#], **Tristan Discroll**[1,#], **Liana C. Boraas**[1], **William Armero**[1], **Dionna M. Kasper**[1], **Nicolas Baeyens**[2,3], **Charlene Jouy**[3], **Venkatesh Mallikarjun**[3,4], **Joe Swift**[3,4], **Sang Joon Ahn**[1], **Donghoon Lee**[5,6], **Jing Zhang**[5,6], **Mengting Gu**[5,6], **Mark Gerstein**[5,6,7], **Martin Schwartz**[1,3,8,*], and **Stefania Nicoli**[1,9,10,*]

[1]Yale Cardiovascular Research Center, Department of Internal Medicine, Section of Cardiology, Yale University School of Medicine, New Haven, CT 06511, USA

[2]Current address: Laboratoire de Physiologie et Pharmacologie, Faculty of Medicine, Université Libre De Bruxelles, Brussels, Belgium

[3]Wellcome Trust Centre for Cell-Matrix Research, Manchester Academic Health Science Centre, University of Manchester, Manchester M13 9PL, UK

[4]Division of Cell Matrix Biology and Regenerative Medicine, School of Biological Sciences, Faculty of Biology, Medicine and Health, Manchester Academic Health Science Centre, University of Manchester, Manchester M13 9PL, UK

[5]Program in Computational Biology and Bioinformatics, Yale University, New Haven, CT 06520, USA

[6]Department of Molecular Biophysics and Biochemistry, Yale University, New Haven, CT 06520, USA

[7]Department of Computer Science, Yale University, New Haven, CT 06520, USA

[8]Departments of Cell Biology and Biomedical Engineering, Yale University

[*]Correspondence should be addressed to MS and SN.

Author contributions.

SN and MS conceived the project. AM and TD performed experiments, analyzed data and AM developed the computational data analysis. WA performed and analyzed zebrafish fin fold regeneration experiments. LB performed and analyzed the experiments in Supplementary Fig 2b and c, Supplementary figure 3b–d and 6. SJA performed cell culture experiments in Supplementary Fig.3a. NB and CJ performed the 3D cell-culture experiments and analyzed the data. DL, MG, JZ, and MG develop the sequence data processing, analysis (mapping, peak calling) of the AGO2-HITS-CLIP experiment. VM and JS performed mass spectrometry proteomic analysis. DMK made the miRNA and RNA-sequencing libraries. AM, TD, MS and SN designed the experiments. MS and SN wrote the manuscript. All the authors edited the manuscript.

[#]These authors contributed equally.

Data Availability

Data availability RNA seq and sRNA-seq data for endothelial cell that support the findings of this study have been deposited in the Gene Expression Omnibus (GEO) under accession codes GSE99686 and GSE11021. sRNA-seq for HDF have been deposited in the Gene Expression Omnibus (GEO) under accession code GSE123008. Data availability for HITS-CLIP data heve been deposited in Sequence Read Archive (SRA) under accession code PRJNA507245. Proteomics data has been uploaded to the PRIDE depository (PXD011882) and results are summarized in Supplemental Table 5. Source data for all Figures and Supplementary Figures have been provided as Supplementary Table 8.

Competing Financial Interests. The authors have no competing financial, professional or personal interests.

[9]Department of Genetics, Yale University School of Medicine, New Haven, CT 06510, USA

[10]Department of Pharmacology, Yale University School of Medicine, New Haven, CT 06510, USA

Abstract

Vertebrate tissues exhibit mechanical homeostasis, showing stable stiffness and tension over time and recovery after changes in mechanical stress. However, the regulatory pathways that mediate these effects are unknown. A comprehensive identification of Argonaute-2(AGO2)-associated microRNAs and mRNAs in endothelial cells identified a network of 122 microRNA families that target 73 mRNAs encoding cytoskeletal, contractile, adhesive and extracellular matrix (CAM) proteins. These microRNAs increased in cells plated on stiff vs. soft substrates, consistent with homeostasis, and suppressed targets via microRNA recognition elements (MREs) within the 3'UTRs of CAM mRNAs. Inhibition of DROSHA or AGO2, or disruption of MREs within individual target mRNAs such as Connective Tissue Growth Factor (CTGF), induced hyper-adhesive, hyper-contractile phenotypes in endothelial and fibroblast cells *in vitro,* and increased tissue stiffness, contractility and extracellular matrix (ECM) deposition in the zebrafish fin-fold *in vivo*. Thus, a network of microRNAs buffers CAM expression to mediate tissue mechanical homeostasis.

Introduction

Cells sense physical forces, including the stiffness of their ECM, through mechanosensitive integrins, their associated proteins, and actomyosin. These components transduce physical forces into biochemical signals that regulate gene expression and cell function[1–3]. Tissues maintain nearly constant physical properties in the face of growth, injury, ECM turnover, and altered external forces (e.g. from blood pressure, tissue hydration or body weight)[1,4,5]. These effects imply tissue mechanical homeostasis, in which cells sense mechanical loads, due to both external and internal forces, and adjust their rates of matrix synthesis, degradation and organization to keep tissue properties constant. Cell contractility is critical in this process, as it is a key component of both the stiffness-sensing regulatory pathways and the matrix assembly process that governs resultant matrix properties, including stiffness[2,6].

Mechanical homeostasis requires that integrin mechanotransduction pathways mediate negative feedback regulation of the contractile and biosynthetic pathways to maintain optimal tissue stiffness. That is, too soft/low force triggers increased matrix synthesis and contractility, while too stiff/high force triggers the opposite. However, *in vitro* studies have mainly elucidated positive feedback (or feed forward) circuits, where rigid substrates or high external forces increase actin myosin contraction, focal adhesions and ECM synthesis[7]. This type of mechanotransduction signaling characterizes fibrotic tissues, where sustained contractility and excessive ECM compromise tissue function. Very little is known about negative feedback pathways that are critical to establish proper stiffness/contractility in normal, healthy tissues.

microRNAs (miRNAs) are processed via the ribonucleases DROSHA/DRG8 and DICER[8] into mature 20–21 nucleotide (nt) RNA that recognize abundant and conserved 7–8 nt

miRNA responsive elements (MREs) within mRNAs. MREs reside mainly in the 3' untranslated regions (3'UTR) of mRNAs and base-pair with the 5' miRNA mature sequence (SEED region)[9]. The miRNA-MRE pairs are recognized by the AGO2 protein complex, resulting in mRNA destabilization and/or reduced protein expression[8]. miRNAs can thus buffer fluctuations in protein levels caused by changes in transcriptional inputs or extracellular factors.

Although miRNAs participate in regulatory feedback loops that contribute to homeostasis in multiple contexts[10–12], their role in mechanical homeostasis is currently untested. Here we describe a miRNA-cytoskeletal-matrix-actin (CAM) mRNA regulatory network that counteracts the effects of the ECM stiffness to promote the mechanical stability of cells and tissues, in both *in vitro* and *in vivo* models.

Results

miRNAs preferentially bind to CAM 3'UTRs.

To investigate potential roles for miRNAs in mechanical homeostasis, we analyzed miRNA-mRNA interactions transcriptome-wide using an AGO2-HITS-CLIP approach[13]. AGO2-bound miRNAs/mRNAs were isolated from two unrelated human endothelial cells (EC) types, which are known to respond to mechanical forces, including ECM loads[3,14]. We exposed cultured human umbilical artery ECs (HUAECs) and human venous umbilical ECs (HUVECs) to UV light to cross-link protein-RNA complexes. Subsequently, we immunoprecipitated AGO2-RNA complexes, digested unbound RNA (schematic in Fig. 1a), and prepared cDNA libraries containing small (~30 nt AGO2-miRNA) and large RNAs (~70 nt AGO2-target mRNA) (Supplementary Fig. 1a). To identify conserved AGO2 binding sites, we performed high throughput sequencing of three libraries for each cell type and selected sequence reads shared in all six samples. We aligned these AGO2 binding sites to human miRNA and genome databases, and identified 30–70 nt interval (peaks) significantly enriched above background (p-value < 0.05, Supplementary Fig. 1a and Methods). This analysis uncovered 316 AGO2-binding peaks within the 3'UTRs of 127 human genes. These peaks were preferentially located right after the stop codon or right before the polyadenylation site (Fig. 1b and, Supplementary Table 1), consistent with the enrichment of regulatory miRNA binding sites that destabilize mRNAs[15]. Importantly, the human AGO2-binding peaks within these 30–70 nt sequences were highly conserved across hundreds of species (Fig. 1b), suggesting functional significance.

Gene ontology (GO) analysis of AGO2-bound transcripts revealed that 73 of the 127 target mRNAs encode actin- and microtubule-associated proteins, focal adhesion proteins, ECM proteins and functionally related regulatory proteins (Fig. 1c, Supplementary Fig. 1b). We termed this group the "cytoskeleton-adhesion-matrix" (CAM) genes. The dramatic enrichment of CAM transcripts in the AGO2 complex is not accounted for by their abundance; indeed, the most transcriptionally active genes in cultured ECs pertained to cell division (Supplementary Fig. 1b), which were under-represented in the identified AGO2-binding transcripts. No significant GO terms were associated with the remaining genes identified from the AGO2-HITS-CLIP.

We then searched for specific MRE sequences in AGO2-peaks localized in the 3'UTRs of the CAM transcripts. We identified 122 miRNA families from AGO2-HITS-CLIP (Supplementary Table 2) that recognize one or more AGO2-CAM MREs (Fig. 1c, Supplementary Table 3). Cytoscape software revealed a highly interconnected network of miRNAs binding to CAM transcripts (Fig. 1c). Altogether, these data reveal pervasive miRNA-mediated post-transcriptional regulation of multiple CAM genes in ECs.

Post-transcriptional regulation of CAM genes is sensitive to matrix stiffness.

CAM proteins are highly conserved and play crucial roles in virtually every cell type as determinants of ECM organization and tissue stiffness[16]. This important function led us to hypothesize that the CAM mRNA-miRNA regulome is mechanosensitive. To test this, we plated ECs on substrates of varying stiffness and used a Sensor-Seq strategy[17] to assess post-transcriptional regulation mediated by 97 selected MREs within 51 different CAM 3'UTRs (Supplementary Table 4). For this purpose, we created a "CAM-sensor library". Each AGO2–3'UTR-peak containing at least one MRE was cloned downstream of an mCherry reporter in a bidirectional lentiviral vector[18] that co-expressed a GFP transcript lacking a 3'UTR (schematic in Fig. 2a). miRNAs that target the MRE thus reduce mCherry levels, leading to a decreased mCherry/GFP ratio. ECs infected with this CAM-sensor library at low levels (to avoid multiply infected cells) were seeded for 48 hours on substrates with rigidity of 3 kPa (kilopascal) or 30 kPa, which approximate "soft" and "rigid" tissues[19], respectively (Supplementary Fig. 2a). miRNA activity on the MRE sensors was compared with the steady state level of CAM proteins, as well as the expression of CAM RNAs and miRNAs, in the same cellular settings. Thus, proteomics, RNA and miRNA sequencing were assessed in parallel.

To evaluate CAM sensor reporters, ECs were separated by fluorescence-based sorting into bins according to the mCherry/GFP ratio, using an empty-sensor as a negative control (not suppressed) and a miR-125-sensor as a positive control (strongly suppressed). Thus, bins were defined as "strongly suppressed", "suppressed", "mildly suppressed", and "not suppressed" relative to these internal standards (Fig. 2b). Wild-type ECs expressing the CAM sensor library showed a broad distribution between the suppressed and not suppressed bins, on both soft and stiff substrates (Fig. 2b). Importantly, CRISPR/Cas9-mediated disruption of AGO2 diminished the miRNA levels in ECs (Supplementary Fig. 2b and c), and significantly increased the population of 'not suppressed' cells (Supplementary Fig. 2d). Thus, miRNAs are required for post-transcriptional inhibition of CAM-sensors.

Sensor vectors from sorted cells were then isolated from each bin and barcoded using PCR primers that recognized each cloned CAM MRE and were compatible with high throughput sequencing. Combining global miRNA profiling (Supplementary table 6) and MRE-reads from Sensor-Seq revealed strong correlations between suppression of CAM sensors and the level of the respective matching miRNAs (Fig. 2c). Notably, both miRNA levels and CAM reporter suppression were present on soft substrate at baseline and elevated in cells on stiff substrates (Fig. 2c). Interestingly, the levels of most CAM mRNA and respective proteins (Supplementary table 5) were also generally higher in stiff conditions (Fig. 2c). These results suggest transcriptional co-regulation between miRNAs and CAM mRNA targets on

stiff substrates. Thus, the CAM MRE-miRNA network has the characteristics of a mechanoregulatory buffer of structural protein coding genes.

Loss of miRNAs biogenesis leads to ECs contractility.

To evaluate the function of this miRNA regulatory network, we first examined ECs lacking AGO2 or DROSHA, which have diminished miRNA levels (Supplementary Fig. 2c and[20]). We stained cells for F-ACTIN, the focal adhesion marker PAXILLIN, and the mechanosensitive transcription factor YAP[21], and also measured traction stresses using elastic substrates with embedded beads[22]. Relative to control cells, AGO2 mutant cells showed increased actin stress fibers, focal adhesions, YAP nuclear localization and traction stress on both 3 or 30 kPa substrates, as well as on polyacrylamide substrates over a wider range of stiffnesses (Fig. 3a and Supplementary Fig. 3a). Consistent with these observations, immunofluorescence analysis revealed that cell spreading and YAP nuclear activation were inversely correlated with AGO2 protein levels (Supplementary Fig. 3b). ECs lacking DROSHA were similarly hyper-adhesive and hyper-contractile, supporting that diminished miRNA levels are the primary cause of these effects (Fig. 3b). Complementary to this finding, proteomic analysis of ECs lacking miRNAs showed increased levels of several CAM proteins, reminiscent of the increased CAM levels in ECs plated on 30 kPa versus 3 kPa substrates (Fig. 3c and Supplementary table 5). Together, these data show that the loss of miRNA-mediated suppression of mRNAs increases CAM protein levels and enhances ECs contractility and adhesion.

Blocking individual CAM-miRNA interactions affects ECs mechanotransduction.

To further validate the function of the miRNA-CAM mRNA network, we disrupted individual CAM-miRNA interactions. We chose nine of the mechanosensitive CAM MREs (stars in Fig. 2c, and Supplementary table 6 in which the MRE was within 20 nt of a protospacer sequence (PAM) and thus targetable by a guide RNA (gRNA) and Cas9. Genome-wide analyses of CAM MREs in ECs treated with gRNA/CRIPSR/Cas9 revealed that nearly 75% of insertions and deletions were within the desired MRE region (±20 base pairs) (Fig. 4a and Supplementary Fig. 4a). To test whether MRE-proximal mutations increased expression of the cognate proteins, we analyzed CAM protein levels via immunofluorescence and Western blot. Individual CAM levels increased in the respective MRE mutants compared to control cells (Fig. 4b), consistent with loss of miRNA-mediated suppression[23].

Finally we tested the mechanical properties of each CAM MRE mutant population and found, to varying extents, that cell area, YAP nuclear localization and/or traction stresses were significantly higher compared to control targeted cells (Fig. 4d).

While multiple genes clearly contributed to each effect, the gene whose MRE mutation gave the most consistent results across multiple assays was *CTGF*. CTGF is a matrix protein that modulates the interaction of cells with the ECM[24], suggesting that it is a component of a protein-based regulatory network and likely functions via receptor-mediated signaling to control these functions. Blocking CTGF miRNA-repression in ECs via a target protector RNA oligonucleotide or MRE mutation had similar effects (Fig. 4d and Supplementary Fig.

4b), providing independent support. Notably, no single CAM MRE mutation reproduced the strong phenotype observed after AGO2 downregulation, suggesting that a network of miRNA-CAM mRNA interactions mediates mechanical homeostasis in cells.

miRNA-dependent regulation limits contractility in 2D and 3D fibroblast models.

We next tested the generality of the identified miRNA-CAM gene regulations using fibroblasts as a second model system. Profiling of miRNAs in Human Dermal Fibroblasts (HDFs) seeded on 3 vs. 30 kPa substrates showed that miRNAs targeting CAM genes are upregulated on stiff substrates similarly to ECs (Supplementary Fig. 5a and Supplementary table 7). Depletion of AGO2 in HDFs also increased F-ACTIN, focal adhesions, traction forces and YAP localization compared to control cells (Fig. 5a and Supplementary Fig. 5b).

To determine if the miRNA-mediated network functions at the tissue level, we examined primary mouse dermal fibroblasts in a 3-dimensional (3D) matrix. Cells suspended in attached fibrin gels contract and replace the fibrin with their own matrix over about 5 days (Fig. 5b), providing a 3D model of cell behavior. Transduction of freshly isolated cells with a CRISPR/Cas9/gRNA virus targeting *Ago2* reduced Ago2 protein levels by ~50–60% (Supplementary Fig. 5c). Ago2-depleted fibroblasts in 3D matrix generated tissue constructs with reduced diameters but no significant change in cell numbers (Fig. 5b). Immunostaining transverse sections of these constructs confirmed the decreased diameter, based on staining with the cytoskeleton protein Vimentin (Fig. 5c). Staining for phosphorylated myosin light chain was elevated, consistent with increased contractility (Fig. 5c). These data suggest that reducing miRNA-dependent regulation stimulates fibroblast contraction of 3D matrix.

miRNA-dependent regulation controls tissue stiffness and wound healing *in vivo*.

We next tested whether miRNAs regulate mechanical homeostasis *in vivo* using the zebrafish fin fold regeneration model[25]. The fin fold is a non-vascularized appendage comprised of a few layers of epidermis and fibroblast-like cells[26]. Wounding triggers a healing response mediated by a conserved and rapid matrix remodeling- and actomyosin-based process that involves formation of a provisional matrix, inflammatory cell invasion, cell migration, proliferation and resolution[27].

To investigate miRNA-dependent regulation of mechanical homeostasis in zebrafish, we first examined embryos that carry a maternal zygotic homozygous mutation in *ago2* (*mz ago2* −/−)[28], which show reduced levels of Ago2 and of miRNAs (Supplementary Fig. 6a). To evaluate miRNA activity in the fin fold, we co-injected an miRNA-sensitive GFP mRNA, containing three perfect miR-24 MREs within the 3'UTR[29], with an miRNA-insensitive mCherry control mRNA. As expected, *mz ago2* mutants showed elevated levels of GFP, but not of mCherry, when compared to wild-type (WT) embryos, confirming reduced miRNA-mediated suppression (Supplementary Fig. 6b).

We then quantified tissue stiffness using atomic force microscopy (AFM)-based nanoindentation on the central region of the fin fold. The appearance of this tissue was indistinguishable between genotypes (Fig. 6a), ruling out obvious developmental defects. However, the elastic modulus was ~30% higher in *mz ago2* −/− than WT embryos, indicating increased mechanical rigidity (Fig. 6a). Importantly, normal tissue stiffness was

restored upon injection of *in vitro* transcribed mRNA encoding human AGO2 (*hsAGO2 mRNA*), demonstrating that the stiffness of this tissue is dependent upon the level of Ago2 (Fig. 6a). Following amputation, *mz ago2* mutants exhibited slower repair than WT embryos, which was rescued by *hsAGO2 mRNA* (Fig. 6b). WT and *mz ago2* −/− wounds did not display differences in cell cycle progression, detected by Proliferating Cell Nuclear Antigen (PCNA) staining[30], or in apoptosis, detected by TUNEL[31] assay (Supplementary Fig. 6 c and d). These results support that miRNA-dependent suppression restrains tissue stiffness and contributes to tissue healing *in vivo*.

miRNA-dependent CAM gene regulation limits tissue contractility during wound healing.

Wounding triggers increased contractility and matrix rigidity as a rapid, first response[32]. According to our notion of mechanical homeostasis, these changes should activate negative feedback mechanisms that restore mechanical equilibrium[3]. We therefore examined matrix, actomyosin activation and the mechanosensitive translocation of Yap[21] before and after wounding the zebrafish fin fold in WT vs. *mz ago2* mutant. As expected[27], WT embryos showed increased staining for pMyosin, Ctgfa and Fibronectin[27,32] in the wound area between 0.5 and 2 hours post amputation (hpa), (Fig. 7a and b, Supplementary Fig.7a). In comparison, *mz ago2* −/− wounded fins showed strikingly elevated and persistent pMyosin staining at both 0.5 and 2 hpa, and higher Ctgfa and Fibronectin at 2 hpa (Fig. 7a and b, Supplementary Fig. 7a). Consistent with the increase in tissue stiffness (Fig. 6a), *mz ago2* −/− showed higher basal Yap nuclear localization compared to WT embryos that further increased at 0.5 hpa and persisted at 2 hpa (Fig.7c and Supplementary Fig. 7b). Thus, loss of miRNA-mediated suppression leads to an exaggerated mechanical response and impaired mechanical resolution during wound healing.

To correlate these effects with regulation of individual CAM genes, we generated zebrafish embryos carrying mutations in the two 3'UTR MREs of the *ctgfa* gene (Supplementary Fig. 7 c and d). These MREs are conserved in the human *CTGF* 3' UTR, and their mutation had the largest effect *in vitro* (Fig. 4c). Accordingly, a GFP sensor mRNA bearing a *ctga* 3'UTR fragment showed reduced expression in WT relative to *mz ago2* −/− embryos, which required the MRE sites (Supplementary Fig. 7c). These results support miRNA-dependent inhibition of *ctgfa* via the MREs in zebrafish. Embryos with mutated *ctgfa* MREs showed persistent p-Myosin activation compared to WT by 2 hpa (Fig. 7b), consistent with the induction of Ctgfa at 2 hpa in the *mz ago2* mutant (Fig. 7a). However, no other differences were detected in the *ctgfa* MRE mutant embryos (Fig. 7a and c, and Supplementary Figs. 6c, d and 7a, b). These results support that post-transcriptional regulation of *ctgfa* contributes to specific Ago2-mediated mechanical effects within the miRNA-CAM mRNA network.

Discussion

We report that an unbiased analysis of miRNAs and their target genes in ECs, together with functional assays in several biological systems, reveal the existence of a mechanosensitive miRNA-based program that counteracts cell adhesion, cytoskeletal, contractile and matrix protein expression. This system functions in several cell types, across multiple species, and appears to be conserved throughout vertebrate evolution. Importantly, most of the protein-

coding genes for synthesis and assembly of stiff ECM are targeted by miRNAs that are upregulated on stiff substrates. Thus, a “buffer” is generated, in which increased matrix stiffness upregulates both cytoskeleton-adhesion-matrix gene transcription and the miRNAs that suppress these transcripts. This miRNA-regulome has the molecular and functional characteristics of a homeostatic mechanism in which changes in cell contraction and matrix are counteracted to maintain normal tissue stiffness (Fig. 7d).

ECs *in vivo* are also subject to wall stretch and fluid shear stress from blood pressure and blood flow, which were not examined here but which are likely to interact with cell responses to matrix stiffness. Interestingly, both of these variables are subject to negative feedback regulation[4], consistent with the general importance of mechanical homeostasis. While the current studies dissected the post-transcriptional regulation of CAM proteins in stiffness homeostasis, a deeper understanding of these mechanisms will need to address the interplay between RNA regulation, stiffness, shear stress in endothelial and other cells subject to external forces.

A network-mediated mechanism for stiffness homeostasis, rather than regulation of one or a few CAM genes, would be expected to increase the robustness of the system. Multiple miRNAs can regulate a large cohort of CAM genes via different MREs, while different cell types can do so by controlling expression and processing of tissue-specific mature miRNAs[33–35]. We speculate, however, that these miRNA networks are likely to be sub-elements within a larger and more robust network of negative and positive circuits, connected by multiple nodes, that mediate tissue homeostasis over the multiple decades of human life[36]. Such nodes could develop within a hierarchy of epigenetic factors in which, for example, the activation of YAP/TAZ and its direct target gene *CTGF*, may be one of the upstream components.

A role for miRNAs in tissue mechanical homeostasis is supported by the widespread de-regulation of miRNAs during lung, renal, cardiac and liver fibrosis, including miRNAs that target ECM proteins[37–39]. Idiopathic lung fibrosis is also linked to reduced levels of miRNAs that target ECM, cytoskeletal and TGFβ pathways genes[40–42]. All of these studies reported reduced levels of miR-29 species, in contrast to our finding that in normal cells, miR-29 species are increased on stiff substrates. These results are consistent with the notion that fibrotic disease involves disruption of normal stiffness miRNA-dependent homeostasis[43].

Cells and tissues with impaired regulation of miRNAs upon AGO2 or DROSHA partial loss of function show defective adaptation to stiffness. The degree of such effects could be related to the corresponding miRNAs levels. Although model organisms that completely lack miRNAs do not develop properly, heterozygous mutants of Ago2 do not manifest obvious phenotypes[44]. Further studies will be necessary to test whether this model has tissue stiffness defects in normal conditions and/or respond abnormally to perturbations such as wounding or during aging.

miRNA-dependent post-transcriptional regulation of structural proteins provides a concrete molecular mechanism that can explain how healthy tissues sustain optimal mechanical

properties. These findings are therefore an important step toward understanding the pathological alterations resulting in fibrotic and related diseases. Characterizing the stiffness-dependent RNA metabolism of cytoskeleton and matrix transcripts, their possible regulation under other physical forces, and elucidating the complete regulatory network that mediates long-term mechanical robustness are the essential tasks for future studies.

Methods

Cell Culture

Human umbilical vein endothelial cells (HUVECs) and human umbilical artery endothelial cells (HUAECs) were purchased from Cell Applications Inc. (Cat # 200–05n and Cat #202–05n). Endothelial cells were cultured on dishes coated with 0.2% w/v gelatin (10 min at room temperature (rt) in PBS, Sigma) in endothelial cell growth medium (EGM Bullet Kit, LONZA). For HITS-CLIP assays, cells were used at P3 (split 1:3 and 1:5) before UV crosslinking. For other assays, cells were split 1:3 twice per week and used until passage 5. Human dermal fibroblasts (HDFs) were purchased from ATCC (Cat #PCS-201–010, Lot# 63014910) and cultured on 0.2% w/v gelatin-coated dishes in fibroblast growth medium (Fibroblast Growth Kit-Low Serum, ATCC, PCS-201–041). HDFs were split 1:10 twice per week and used until passage 6.

Primary fibroblasts

Primary dermal fibroblasts for 3D fibrin gel assays were obtained from 5 to 8 week old C57BL/6 mice (Envigo, UK). This study is compliant with all relevant ethical regulations regarding animal research. All procedures were in accordance with UK Home Office regulation and UK animals (Scientific Procedures) Act of 1986 for the care and the use of animals. Mice were sacrificed by a schedule 1 procedure by trained personnel. Mouse hair was removed and skin dissected in Hank's buffer supplemented with antibiotic and antimycotic solution (Sigma). Fat and excess connective tissues were removed, the dermis was minced with a scalpel and digested in buffer containing 0.25% trypsin without EDTA (Gibco), collagenase IV (4 mg/mL (Worthington) and calcium chloride (0.3 mg/mL, Sigma) for 3 h at 37 °C with agitation during the last hour. After mechanical dissociation, cells were passed through a cell strainer (100 μm, Fischer Scientific). Cells were centrifuged at 1800 rpm for 5 min, resuspended in DMEM supplemented with 10% Fetal Bovine Serum (Sigma), Penicillin (100U/mL), Streptomycin (100 ug/mL) (Gibco) and 1% L-glutamine, and seeded in 75 cm^2 tissue culture flasks. Medium was changed at 3 h and subsequently changed once a day.

AGO2-HITS-CLIP

HITS-CLIP experiment was performed as previously described[47]. Sub-confluent endothelial cells (ECs) in EGM were UV crosslinked two times with 400 mJ/cm^2 in Stratalinker (model 2400, Stratagene), lysed and treated with DNase (1:1000 Promega RQ1 DNase) and RNase T1 (1:100, Thermo Fisher). Cell lysates and Protein A Dynabeads (Invitrogen) complexed with Ab-panAGO-2A8 (MABE56 Millipore) were incubated at 4°C for 4 h. Beads were subsequently washed and ligated with 3' -P32 radiolabeled linker (RL3, Supplementary table 6). SDS-PAGE was performed using NuPage 4–12% Bis-Tris Gel (NP0321

Invitrogen), and proteins were transferred onto Pure Nitrocellulose membrane (BioTrace) using NuPAGE transfer buffer according to manufacturer's instructions. High performance autoradiography film was exposed overnight at −80°C. The bands corresponding to AGO2-miRNAs (~110 kDa), and AGO2: RNA (~130 kDa) were cut and treated with proteinase K (Roche) to degrade proteins. RNAs were extracted and purified via phenol-chloroform, then a 5'-linker oligonucleotide (RL5, Supplementary table 6) was ligated to the ends. cDNA libraries were generated using DNA oligos complementarity to RL3 and SuperScriptIII reverse transcriptase (Invitrogen). Products were then PCR amplified using specific primers (DP5, DP3, Supplementary table 6) and purified via agarose PAGE 1% using a Gel extraction kit (Qiagen). A second round of PCR was performed, using custom Illumina Hi-Seq primers with three different barcodes to multiplex the libraries (DSFP5, DSFP3-Index1, DSFP3-Index4, DSFP3 -Index8, Supplementary table 6). Products were PAGE purified using the Gel extraction kit, and libraries were analyzed by the YCGA Sequencing facility using a customized Illumina primer (SSP1, Supplementary table 6).

HITS-CLIP Data Analysis

Prior to aligning sequencing reads, the raw data were analyzed for quality steps to reduce artifacts: adapters were removed from raw reads, filtered according to quality scores and exact sequence duplicates were collapsed. Remaining reads were aligned using STAR RNA-seq aligner (version 2.4.1a)[48] using UCSC hg19 reference human genome. A minimum of 10 bases matched was enforced, only unique reads were used, and a maximum of 3 mismatches were allowed. Replicates were merged using Samtools (version 1.2)[49] and the aligned reads were analyzed with Piranha using a bin size of 30 bp. All identified peaks with p-value less than 0.05 were mapped to Gencode version 22 annotation.

Conservation between artery and vein samples was calculated for each identified peak using PhastCons 100 conservation scores. Using Piranha peaks setting, a Wilcoxon rank sum test was performed to compare the difference in distribution of conservation score across samples.

For microRNA identification, reads were aligned using Novoalign (Novocraft, http://www.novocraft.com/products/novoalign/) against human microRNA sequences from miRBase (release 21)[50]. The miRNA expression levels were quantified as reads per million (RPM). Endothelial microRNAs identified in AGO2-HITS-CLIP were divided into families based on 8mer SEED regions.

Using TargetScan software[51], these microRNA SEED families were associated to the AGO2-HITS-CLIP peaks based on the putative MRE.

To test expression of CAM vs. other genes in cultured ECs, we examined previously published microarray data performed in freshly isolated versus cultured HUVEC and HUAEC (GEO ID: GSE43475)[52]. Standard microarray analysis for differential gene expression (DEG) was performed using packages simplyaffy (http://bioinformatics.picr.man.ac.uk/simpleaffy/) and limma[53] from Bioconductor (http://www.bioconductor.org/).

CRISPR/Cas9 strategy to generate mutant primary cells

To mutate *AGO2* in HUVECs and HDFs, a pLentiCRISPR vector containing an AGO2 or a non-targeting guide RNA (control, which doesn't target know mouse or human genome sequences) was used (Supplementary table 6). Lentiviruses were generated by transfecting Lenti-X 293T cells (Clontech) with packaging vectors (2.5 μg VSV; 5μg pxPAX2, Addgene) and the pLentiCRISPR DNA vector (7.5ug) using lipofectamine 2000 (Invitrogen). Virus containing supernatant was collected 36 and 60 h post transfection. In Supplementary Fig. 2b shows a schematic of approach. Cells were infected with pLentiCRISPR virus containing AGO2 gRNAs or non-targeting gRNAs in the presence of polybrene (8 μg/ml). To generate cells with mutant MREs, similar vectors were generated to target the selected MRE sequences identified in the AGO2 HITS-CLIP experiment and confirmed via Sensor-seq. The complete lists of genes and gRNAs are reported in Supplementary table 6. Cells were cultured for 7–10 days (up to a maximum of passage 5) prior to seeding on gels for immunostaining or traction force microscopy. Reduced AGO2 expression was confirmed by Western blot at 7 and 10 days post-infection. Cells were lysed in RIPA buffer with protease and phosphatase inhibitor cocktail (Roche) on ice. Samples were loaded onto 8% or 4–12% SDS-PAGE gels, transferred on Immun-Blot PVDF membrane (Biorad), blocked with 10% milk for 2h and incubated with rabbit anti-AGO2 (Cell Signaling, 1:2000) and mouse anti-β −Actin (Santa Cruz) overnight at 4°C. Secondary antibody incubation was done with anti-mouse-HRP and anti-rabbit-HRP (Santa Cruz, 1:4000) for 1h. For blots of other proteins following MRE mutation, target protector or knockdown, membranes were blocked with 5% w/v BSA in PBS 0.1% Tween for 1 hour and incubated with primary antibody for RhoB (1:200, sc-8048, Santa Cruz), CTGF (1:1000, ab6992, Abcam), Vinculin (1:2500, V9131, Sigma-Aldrich), STMN1 (1:10000, ab52630, Abcam), DROSHA (1:5000, ab183732, Abcam), or GAPDH (1:4000, 2118, Cell Signaling) overnight at 4°C. After washing, membranes were incubated with secondary antibody anti-rabbit-HRP or anti-mouse-HRP (1:4000, 7076P2 and 7074S, Cell Signaling) for 1 hour at rt in 5% BSA TBS-T. After washing, blots were developed with super signal west pico chemiluminescent substrate (Thermo) using a SYNGENE G-Box imager.

Single amplicons of ~300 bp were generated using primes equidistant from the putative region of mutation. PCR amplicons were combined and sent to Yale Sequencing Facility for MiSeq 2×250 analysis. After sequencing, single amplicons were demultiplexed and single reads were used for msa (Multiple sequence alignment) against the wild-type sequence using R msa package[54]. The frequency of each mutation was calculated as total reads for each CAM gene mutation divided the sum of all the reads aligned to specific CAM gene, and plot as bar plot.

To mutate *Ago2* in mouse fibroblast, pLentiCRISPRV2 (Addgene) vectors containing Ago2 or non-targeting guide RNAs (control, as above) were used. P0 fibroblasts at 80% confluence were infected with lentivirus containing either non-targeting or Ago2 guide RNA in the presence of 4mg/mL polybrene for 16 h. Culture medium was changed and cells were incubated for 72 h. Infected cells were selected in medium with 0.5 ug/mL puromycin for 48 h (this concentration efficiently kills all control cells) and then cultured for another 96 h before use in matrix constructs. Reduced Ago2 expression in mouse fibroblasts constructs

was confirmed by Western blot at 5 days. Matrix constructs were washed with cold PBS, frozen in liquid nitrogen, then homogenized with metallic beads in a Bullet Blender (Strom 24, Next Advance) in protein extraction buffer (1.1% Sodium dodecyl sulphate, 0.3% sodium deoxycholate, 25mM dithiothretol, in 25mM ammonium bicarbonate with Complete anti-protease and anti-phosphatase, Roche). Protein samples were loaded in a 4–12% Nu-Page pre-casted gel (ThermoScientific) for electrophoresis (200V, 50 min), transferred to nitrocellulose membrane (Biorad), blocked for 1 h with Odyssey PBS blocking buffer (LiCor biosciences) and incubated overnight with antibodies against Ago2 (Cell Signaling, 1:2000) and beta-actin (Abcam 1:5000). After washing in PBS-Tween, membranes were incubated with AlexaFluor-680 anti-mouse and AlexaFluor-800 anti-rabbit (both from Thermo, 1/15000). Membranes were scanned with an Odyssey CLX NIR scanner (Licor biosciences) and fluorescence intensity of the bands quantified with the Image Studio software (Licor biosciences).

shRNA knockdown of DROSHA and miRNA Target Protector for CTGF

Knockdown of DROSHA was performed using Dharmacon shRNA SMARTvectors (GE Healthcare). Lentivirus was prepared in Lenti-X 293T cells as before using a non-targeting negative control shRNA and two shRNAs directed at DROSHA (Neg Control shRNA, shDRO#1, shDRO#2, Supplementary table 6). Experiments were performed with shDRO#2 (~95% knockdown at 5 days). DROSHA knockdown was verified by immunoblot as before with DROSHA antibody (Abcam, ab183732, 1:5000).

Disruption of the miRNA-MRE interaction with the CTGF gene was performed using a miScript Target Protector (Qiagen) directed at the MRE within the human CTGF gene. The CTGF target protector (CTGF_1_TP, Cat#MTP0079186) or the Negative control target protector (Cat#MTP0000002) were transfected into P2 HUVECs at 20nM using Lipofectamine RNAiMax (Invitrogen) in OPTI-MEM (Gibco) with 4% FBS (Sigma) twice (1 and 3 days post seeding). CTGF increases post transfection were verified by immunoblot as before with a CTGF antibody (Abcam, ab6992, 1:1000).

PDMS and Polyacrylamide Substrates

Polydimethylsiloxane (PDMS) substrates were cast in the bottom of 10cm tissue culture dishes or #1.5 cover-glass bottomed 35mm Mattek dishes (for imaging studies). Soft (3kPa) gels were made using a 1:1 ratio (by weight) of PDMS component A and B (CY 52–276 A and B, Dow Corning), degassed for 30 min in a vacuum desiccator, and cured for 24 h at rt. Stiff (30kPa) gels were made using a 40:1 ratio (by weight) of Sylgard 184 components B and C (SYLGARD 184, Dow Corning), degassed for 30 min and cured for 3 h at 70°C. Prior to seeding, gels were washed with PBS, sterilized with UV for 20 min, and coated with bovine plasma fibronectin (10μg/ml in PBS) overnight at 4°C.

Polyacrylamide gels were prepared using a protocol modified from previously published methods[55]. Briefly, 30-mm glass bottom dishes were activated with glacial acetic acid, 3-(trimethoxysilyl) propyl methacrylate, and 96% ethanol solution (1:1:14 ratio, respectively) for 10 min at rt. For fibronectin protein conjugation (1mg/ml) on the polyacrylamide gel, acrylic acid N-hydroxysuccinimide ester was partially mixed as a substitute of acrylamide.

Each stiffness was prepared with the ratio shown in Supplementary Table 9 which was previously reported[55].

RNA, miRNA and Sensor-seq library preparation

Total RNA was extracted from three replicates of cultured HUVEC or HDF cells seeded on 3kpa or 30kpa PDMS using TRIzol reagent (Life Technologies) according to the manufacturer's protocol. For mRNA libraries, total RNA was treated with DNA-free DNase (Ambion) and 500 ng of treated RNA was used to prepare Lexogen QuantSeq 3′ mRNA-Seq FWD libraries for Illumina deep-sequencing according to the manufacturer's protocols. Libraries were amplified with 12 PCR cycles. miRNA libraries were prepared from 1μg of total RNA using the NEBNext® Small RNA Library Kit (NEB) following the gel size selection method in manufacturer's protocol and submitted for Illumina sequencing. For Sensor-Seq library, a customized oligonucleotide library was synthetized by Integrated DNA Technologies (IDT). The sequence of each individual oligonucleotide was obtained from Piranha analysis (see Supplementary Table 4) extending the genomic coordinate of each peak by 20 nucleotides at the 3' and 5' region. 97 peaks with at least 1 predicted MRE, representing 51 CAM genes were selected. In addition, all sensor oligonucleotides contained restriction enzyme sites, AscI and NheI, allowing for PCR base amplification and cloning. The oligonucleotide library was resuspended in 480 μl of water, diluted 1:100 and PCR amplified using Phusion HotStart II HF kit and AscI forward and NheI reverse primers (Supplementary table 6). PCR-amplified libraries were purified using a PCR purification kit (Qiagen) and double digested for 2 h at 37°C.

Sensor-seq backbone[56] containing a bidirectional promoter for UbC upstream of copGFP and mCherry genes, was kindly provided by Dr. Jun Lu, Yale University. After sensor backbone digestion with AscI and NheI, the MRE oligo library was cloned into the 3'UTR of mCherry. Ligation using T4 DNA Ligase (Promega) was incubated 16 h at 16°C, then transformed into DH5α, and pooled colonies were used to prepare a library Maxi prep (Qiagen).

Lentiviruses for expression of the CAM-MRE Sensor library were generated as above using Lenti-X 293T cells. For FACS analysis additional control lentiviruses expressing GFP alone, mCherry alone, miRNA sensor lacking a MRE (Empty-Sensor plasmid, negative control), and miRNA sensor with a synthetic MRE for miR125 (miR125-Sensor plasmid, positive control) were used.

RNA and miRNA seq data analysis

Total RNA and microRNA were aligned against the human genome version GRCh38 using the GENCODE 22 transcript annotation, using STAR alignment software with same parameters used for the ENDOCE project (www.encodeproject.org)

After alignment, differential gene expression (DEG) of RNAs or miRNAs between ECs seeded on 30 and 3 kPa substrates was computed using the negative binomial distributions via edgeR using standard parameter Genes[57,58]. The levels (log 2 Fold Change) of CAM RNAs and SEED matching miRNAs to CAM-MRE sensors, were combined and represented in the CIRCOS plot.

FACS and Sensor-Seq Analysis

For FACS experiments, cells were infected with low levels of the library or control lentivirus in the absence of polybrene to avoid multiply infected cells (10–20% of cells infected). After 48 h, cells were trypsinized and seeded onto soft (3kPa) or stiff (30kPa) fibronectin-coated PDMS dishes at low density (150k cells per 10cm dish) for 2 days. Cells were then washed once with PBS, trypsinized, centrifuged for 5 min at 300xg, and re-suspended in PBS at 500k cells per ml immediately before FACS analysis. Infected cells were sorted on a BD FACSAria II and analyzed with FACSDiva 7. Four sorting gates were set based on the 2 control plasmids (Empty-Sensor and miR125-Sensor). The upper limit bin (Not Suppressed) was designed to contain 90% or more events/cells infected with the Empty-Sensor and less than 0.5% of events for the miR125-Sensor. Conversely, the lower two bins (Strongly Suppressed and Suppressed) were designed to contain 90% of events coming from cells infected with miR125-Sensor, in a ratio close to 3:2 (~60% of events in Strongly Suppressed bin and ~40% of events in Suppressed). The 3rd bin (Mildly Suppressed) was set between the Not Suppressed and the Suppressed bins. For clarity, the contour plot represents the total percentage of event in each single bins, grouped in “island” of 15% probability were shown for the Empty-Sensor, miR125-Sensor, Sensor-Library at 3 kPa and Sensor-Library at 30 kPa.

After sorting of cells into each bin, genomic DNA was isolated using the DNeasy Blood & Tissue Kit (Qiagen) and the MREs were PCR amplified using specific forward primers to barcode each bin (strongly suppressed, suppressed, mildly suppressed, not suppressed, and a reverse primer, Supplementary table 6). The PCR was performed using Phusion HotStart II HF with melting temp of 59°C for 20 sec. Library were purified using gel extraction kit (Qiagen). The primers used contain barcodes for multiplexing and were designed to hybridize with Illumina sequencing.

Computational analysis of Sensor-seq was performed using R. First, the number of reads for each sensor-MRE was divided by the total number of reads in the entire experiment and multiplied by one million to get the Reads Per Million (RPM) for each sensor. To calculate the frequency of sensor-MREs in each bin, the RPM was divided by the total RPM for all 4 bins of the experiment for that sensor, giving frequency values for each MRE in each bin at each stiffness. MREs that showed a dominant bin (with frequency values above 0.375, i.e. non-random) were compared at 3 vs. 30 kPa. In Figure 2c CAM MREs were then plotted based on the reproducible tendency to be enriched in the same bin at a given stiffness but not the other for 3 independent experiments. MREs that shifted towards a more suppressed bin on 30kPa compared to 3kPa were plotted as CAM-MRE 30kPa (bottom left of plot). MREs that that shifted towards a more suppressed bin on 3kPa compared to 30kPa were plotted as CAM-MRE3kPa (upper right of plot). RNA-seq (red) and Proteomics (green) data for each of these proteins was plotted and linked with the miRNA-seq (for miRNAs predicted to bind these MREs). The regulation of CAM-MREs by miRNAs (stars, Figure 2c) was further validated by individual MRE mutagenesis followed by functional assays.

Mass spectrometry (MS) sample preparation and analysis

Cell pellets were lysed in 50 μL of 25 mM ammonium bicarbonate (AB, Fluka) buffer containing 1.1 % sodium dodecyl sulfate (SDS, Sigma), 0.3 % sodium deoxycholate (Sigma), protease inhibitor cocktail (Sigma) and phosphatase inhibitor cocktail (Merck). Six 1.6 mm steel beads (Next Advance) were added and samples were homogenized with a Bullet Blender (Next Advance) at maximum speed for 2 min. Homogenates were subjected to centrifugation (12 °C, 10000 rpm, 5 min). Lysates were added to 150 μL of digest buffer (1.33 mM $CaCl_2$, Sigma, in 25 mM AB) containing immobilized trypsin beads (Perfinity Biosciences) and shaken at 1400 rpm overnight at 37 °C. The resulting digests were reduced with 4 μL of 500 mM dithiothreitol (DTT, Sigma, in 25 mM AB; 10 min. shaking, 1400 rpm, 60 °C) and alkylated with 12 μL of 500 mM iodoacetamide (Sigma, in 25 mM AB; 30 min. shaking, dark, rt). Trypsin beads were removed by centrifugation (10000 rpm, 10 min). Supernatant were transferred to 1.5 mL 'LoBind' Eppendorf tubes and acidified with 5 μL 10 % trifluoroacetic acid (Riedel-de Haën) in water, and cleaned by two-phase extraction (3 × addition of 200 μL ethyl acetate, Sigma, followed by vortexing and aspiration of the organic layer). Peptides were desalted with POROS R3 beads (Thermo Fisher) using the manufacturer's protocol and lyophilized. Peptide concentrations were measured by spectrophotometer (Direct Detect, Millipore) and adjusted to 200 ng μL^{-1} in injection buffer (5 % HPLC grade acetonitrile, ACN, 0.1 % trifluoroacetic acid in deionized water, Fisher Scientific). LC-MS/MS was performed using an UltiMate 3000 Rapid Separation liquid chromatography system (RSLC, Dionex Corporation) coupled to a Q Exactive HF mass spectrometer (Thermo Fisher). Peptides were separated using a multistep gradient from 95 % A (0.1 % formic acid, FA, in water, Fisher Scientific) and 5 % B (0.1 % FA in ACN) to 7 % B at 1 min, 18 % B at 58 min, 27 % B at 72 min and 60 % B at 74 min at 300 nL min^{-1}, using a 75 mm × 250 μm inner diameter 1.7 μM CSH C18, analytical column (Waters). Peptides were selected for fragmentation automatically by data dependent analysis.

Mass spectrometry (MS) data processing and protein quantification

All sample spectra were aligned using Progenesis QI (Nonlinear Dynamics) with manual placement of vectors where necessary. Default parameters were used except where noted. Peak-picking sensitivity was set to 4/5. Peptides with charges between +1 and +4, with 2 or more isotopes, were selected for analysis. Peptide identities were assigned using Mascot (Matrix Science), searching against the SwissProt and TREMBL mouse databases. The database was modified to search for cysteine alkylation (monoisotopic mass change, 57.021 Da), oxidized methionine (15.995 Da), hydroxylation of asparagine, aspartic acid, proline or lysine (15.995 Da) and phosphorylation of serine, tyrosine or threonine (79.966 Da). A maximum of 2 missed cleavages was allowed. Peptide intensities were exported as Excel (Microsoft) spread sheets for processing with Matlab (The MathWorks). Peptide identifications were filtered via Mascot scores, selecting only those with a Benjamini-Hochberg false discovery rate (FDR) < 0.05. Raw ion intensities from peptides belonging to proteins with fewer than 2 unique (by sequence) peptides per protein in the dataset were excluded from quantification. Peptides from CAM proteins were only used for quantification if they were unique to the protein (i.e. did not overlap with other protein sequences). Intensities were logged and normalized by the median logged intensity. Missing values were assumed as missing due to low abundance, as described[59]. Imputation was performed at the

peptide level using a method similar to Perseus[60] whereby missing values were imputed randomly from a normal distribution centered on the apparent limit of detection for the experiment. The limit of detection was determined by taking the mean of all minimum logged intensities and down-shifting it by 1.6σ, where σ is the standard deviation of minimum logged peptide intensities. The width of this normal distribution was set to 0.3σ as described in[60]. Fold-change differences in protein quantities were calculated by fitting a mixed-effects linear regression model for each protein with Huber weighting of residuals as described in[59] using the *fitglme* function (MatLab) with the formula:

$$y_{ipt} = \beta_0 + X_p\beta_p + X_t\beta_t + \varepsilon_{ipt}$$

Where Y_{iptb} represents the $\log_2$(intensity) of peptide p belonging to protein i, under experimental treatment t. βs represent effect sizes for the indicated coefficients. *Peptide* effects were considered as random effects whereas *treatment* was considered as a fixed effect. β_0 denotes the intercept term and ε_{pt} denotes residual variance. Standard error estimates were adjusted with Empirical Bayes variance correction according to[61]. Conditions were compared with two-sided Empirical Bayes–adjusted t-tests with Benjamini-Hochberg correction for false positives.

Cells Immunostaining and Quantification

Cells seeded on fibronectin-coated PDMS were fixed with 4% paraformaldehyde (Electron Microscopy Sciences) in PBS. Cells were then washed and permeabilized with 0.05% Triton X-100 in PBS, with 320 mM sucrose and 6 mM $MgCl_2$. Cells were PBS washed 3 times, blocked for 30 min with 1% BSA in PBS, then incubated overnight at 4°C with anti-YAP antibody (1:200, no sc-101199, Santa Cruz Biotechnology), anti-RhoB (1:250, 19HCLC, ThermoFisher), anti-Vinculin (1:200, V9131, Sigma-Aldrich), anti-STMN1 (1:200, ab52630, Abcam), anti-CTGF (1:200, ab6992, Abcam) and anti-paxillin (1:800, RabMAb Y113, ab32084, Abcam) diluted in 1% BSA in PBS. Cells were washed 3 times with PBS and incubated at rt for 1 hour with secondary antibodies (alexa-488 anti-rabbit, alexa-647 anti-mouse, 1:1000, ThermoFisher) and alexa-565 conjugated phalloidin (1:1000, molecular probes). Cells were washed 3 times with PBS and mounted with DAPI in Fluoromout-G (SouthernBiotech). Cell areas were quantified using ImageJ by background subtracting, thresholding to generate cell masks, and using the analyze particles function. YAP staining was quantified by taking the average nuclear YAP signal (in the area of the DAPI stain), divided by the average cytoplasmic YAP signal (in the area of the non-nuclear cell mask). Focal adhesions were analyzed using the focal adhesion analysis server[62] with the minimum adhesion size set to 0.5 μm^2 and the default settings for only static properties. Average number of focal adhesions per cell was calculated for each field of view by dividing the total number of adhesions in the field by the number of cells.

Traction Force Microscopy

PDMS TFM substrates were fabricated as described[63]. Briefly, cover-glass bottom dishes were spin-coated to obtain a ~40μm thick layer of polydimethylsiloxane (PDMS; Sylgard 184 by Down Corning mixed at various B/C ratios, 67:1 3kPa, 40:1 30kPa) and cured at

70°C for 3 h. Gels were then treated with 3-aminopropyl trimethoxysilane for 5 min and incubated for 10 min at rt with 40nm Alexa Fluor 647 beads (Molecular Probes) suspended in a 100μg/ml solution of 1-Ethyl-3-(3-dimethylaminopropyl) carbodiimide (Sigma) in water to covalently link the beads to the gel surface. Elastic moduli for each batch was measured using a microfluidic device as described[63] and is reported as the Young's modulus (E).

TFM gels were coated with fibronectin (10μg/ml) in PBS overnight at 4°C and washed 3 times with PBS. HUVECs and HDFs were seeded on the gels in EGM or low serum fibroblast growth medium, respectively, 24h before analysis at low density (~3000 cells per cm^2). Cells and florescent beads were imaged on a spinning disk confocal microscope (UltraVIEW VoX, Perkins Elmer) attached to a Nikon A-1 microscope equipped with a temperature and CO_2 controlled incubation chamber and 60× 1.4NA lens. Florescent images of Alexa Fluor 647 beads and DIC images of cells were acquired before and after cell lysis with 0.05% SDS. Images were drift corrected and bead displacements were quantified as described[64]. Force fields and traction stresses were calculated using FTTC force reconstruction with the regularization parameter set to 0.007. Total force per cell was calculated as the average stress under the cell multiplied by the area.

3D matrix constructs

A method to generate 3D cell-derived uniaxial matrix constructs (3D matrix constructs) based on the "tendon construct" developed by Karl Kadler's group was used[65]. Six well plates were coated with a 2 mm layer of SYLGARD 184 and incubated overnight at 65°C to induce polymerization. After cooling, the (hydrophobic) SYLGARD layer was incubated 15 min with Pluronic® F-127. Custom-made rectangular Teflon molds (15×10×2mm) were sterilized with Virkon (10 min) then Ethanol 70% (15 min). Inside the molds, two 8mm segments of size 0 silk sutures were pinned to the PDMS using insect pins exactly 10mm apart. Inside each mold, we added 12 μL of thrombin stock solution (200U/mL, Sigma). Primary fibroblasts were detached with 0.05% trypsin, centrifuged at 1800 rpm and counted. For each matrix construct, 2×105 cells were resuspended in 300 μL of DMEM containing 8mg/mL fibrinogen (Sigma) and 0.2 mM of L-ascorbate-2- phosphate. Cell suspensions were injected inside the molds and placed at 37°C for 15 min in incubator for polymerization. After polymerization, the Teflon mold was removed and one additional insect pin added to maintain the suture thread. Matrix constructs were cultured with DMEM/F12 supplemented with 10% fetal bovine serum (Sigma), Penicillin (100U/mL), Streptomycin (100 ug/mL, Gibco), 1% L-glutamine and 0.2mM of L-ascorbate-2-phosphate. The 3D matrix constructs were cultured for 5 days and the culture medium changed every other day. After 5 days, photographs of the constructs were taken with a Nikon reflex camera equipped with a 50mm macro-objective at a focal distance of 1:1. Constructs diameter was obtained by averaging the diameter at 3 different locations (each extremity and the middle).

Immunostaining matrix constructs

Matrix constructs were rinsed in cold PBS and fixed overnight at 4^oC in 4% formaldehyde (Pierce 16% formaldehyde, methanol free) in PBS. Fixation constructs were dehydrated, embedded in paraffin and 5 μm transverse sections cut with a Leica microtome. For

immunostaining, we performed a rehydration protocol followed by antigen retrieval for 30 min at 96°C in a citrate buffer (pH 6). Sections were blocked with Odyssey PBS blocking buffer (LiCor biosciences) for 1 hour and incubated overnight with primary antibodies diluted in blocking buffer: vimentin (1/400, Cell Signaling), phospho-myosin light chain (1/400, Abcam). After extensive rinsing in PBS Tween 0.1%, slides were incubated with AlexaFluor 647 anti-rabbit secondary antibody (1/500, ThermoScientific) for 1 hour at rt, thoroughly washed with PBS Tween 0.1%, and slides mounted in FluoromountG-DAPI (Southern Biotech). Slides were imaged with an Olympus slide scanner microscope equipped with a 20x objective.

Zebrafish Fin Fold Regeneration

This study is compliant with all relevant ethical regulations regarding animal research. Zebrafish were raised and maintained at 28.5°C using standard methods and according to protocols approved by Yale University Institutional Animal Care and Use Committee (IACUC # 2017–11473). Wild-type (AB) and mz *ago2* −/− mutants[66] were used. To generate the ctgfa MRE mutant, zebrafish AB were injected with 125 ng/µl *Cas9* mRNA and 75 ng/µl gRNAs, designed as previously described[67]. The gRNA sequence used to target the conserved MRE within the 3'UTR human *CTGF* gene was (CTGF MRE gRNA, Supplementary table 6). Genomic DNA was isolated from a clutch of 15 injected and uninjected control embryos at 24 hpf using the Qiagen DNeasy Blood and Tissue Kit. Genomic DNA (250 ng) and the Phusion HotStart II Kit (ThermoFisher) used to PCR amplify an approximately 300 bp region surrounding the intended MRE target (MRE Fw Amp, MRE Rv Amp, Supplementary table 6). T7 Endonuclease I assay was used to detect mutations as described in the manufacturer's protocol (New England BioLabs). PCR and T7 products were run on 3% agarose gels to verify the occurrence of indels in the MRE sequence. The remaining embryos were grown to 48 hpf and used for the fin fold regeneration experiments (see below).

The zebrafish miR-124 and ctgfa sensor assay and mRNA injection were performed as described[67]. For the fin fold regeneration assay, we use 14 AB fish, 14 mz ago2 mutant −/− embryos and 15 mz ago2 −/− fish injected at the one cell stage with 200 pg of in vitro transcribed mRNA encoding the human AGO2 protein. At 2 days post fertilization (dpf), the fin fold was cut at the edge of the fin using a 25G needle. Bright filed images were captured at 0.5, 2, 4, 24, 48 and 72 h post amputation (hpa) using a Leica M165 FC stereomicroscope and Leica Application Suite V4 software. The length of the fins over time was measured using FIJI-ImageJ[68,69] and normalized for the length of the fin before cutting.

Zebrafish immunofluorescence assay

For the fluorescent images: 20 embryos for each genotype (AB, Ago2 mutant (−/−) and ctgfa 3' UTR mutant) were cut and then, at 0.5, 2, 4, 24 hpa were fixed in PFA 4% overnight at 4°C. Embryos were washed 4–5 times with PBS 0.1%Tween, then incubated 2 h in blocking solution (0.8% Triton-X, 10% normal goat serum, 1% BSA, 0.01% sodium azide in PBS Tween). Zebrafish were stained following the protocol as in[70] using the primary antibody mouse anti-Phospho-Myosin Light Chain 2 (1:200; Cell Signaling), mouse anti-Proliferating Cell Nuclear Antigen (1:200; PCNA, Dako), rabbit anti-Fibronectin (1:200;

Sigma), DAPI (1:1000; Sigma), rabbit anti-Connective Tissue Growth Factor A (1:150; Abcam), and mouse anti-YAP (1:200; Santa Cruz Biotechnology) and the secondary antibody Alexa Fluor 488 anti-mouse (1:250, ThermoFisher) and Alexa Fluor 596 anti-rabbit (1:250, ThermoFisher). After staining, images were captured using a Leica Microsystems SP5 confocal microscope using a 40X objective. Max projections were generated and intensity was quantified using FIJI-Image. For each protein staining the intensity profile of 4 to 6 fish was calculated for a section of 80 μm in diameter within the wound and 50 μm from the fin fold edge. Ratio of Nuclear to Cytosolic YAP was calculated before and during the fin fold regeneration from confocal images thresholded using the DAPI channel to generate a binary mask for the nuclei. Using ImageJ, the binary mask was used to generate a nuclear and a cytosolic YAP image. Each was ratioed and normalized to the area. For TUNEL assay to detect apoptotic cells embryos were fixed in 4% PFA overnight and stored in 100% methanol at −20 °C. The TUNEL assay was performed using the ApopTag Red *In situ* Apoptosis Detection kit (Millipore).

Atomic Force Microscopy

Live zebrafish embryos (48 hpf) were anesthetized using 1x tricaine in egg water and mounted on PDMS gels. The tips of fish tails were probed using a DNP-10 D tip (Bruker, nominal stiffness ~0.06 N/m) on a Bruker Dimension FastScan AFM immersed in egg water containing 1x tricaine. Probe deflection sensitivity was calibrated by taking indentation curves on glass and the nominal tip stiffness was calibrated by thermal tuning (assuming a simple harmonic oscillator in water). Force vs. deflection curves were collected for a ramp size of 1.5μm at a rate of 750 nm/s for at least 2 locations per fish, with 10–11 fish measured per group. The first 600nm of the extension curves were fit with NanoScope Analysis Software version 1.5 (Bruker) assuming a Poisson's ratio of 0.5 and using the Sneddon fit model[71].

Statistics and Reproducibility

All the of statistical analysis were performed using Prism version 7.01 (GraphPad) and R, except for the peak identification, which used piranha software[72] to measure the significance of read coverage height for each mapped position using the zero-truncated negative binomial model (ZTNB). To confirm changes in cell area, focal adhesion number, YAP localization and traction force generation, t-tests were performed using Prism to assess the change in the mean between Wild-type and AGO2 or MRE CRISPR/Cas9 mutant cells. These data sets contained more than 20 individual measurements for each condition and showed a log-normal distribution. For *in vivo* analysis of zebrafish wild-type and Ago2 mutants, changes in fin fold tissue were analyzed using t-tests; fin fold regeneration was analyzed via 2 way ANOVA and Sidak's multiple comparisons test for 4 to 6 individual fish for data-set using Prism. Figure legends indicate exact number of measurements, number of independent experiments, and statistical test used for each analysis performed.

Supplementary Material

Refer to Web version on PubMed Central for supplementary material.

Acknowledgements.

We thank Meredith Cavanaugh for help with zebrafish husbandry. We thank the Wellcome Trust Centre for Cell-Matrix Research for technical support with tissue culture assays. We thank Melanie Trombly and Angela Andersen, Life Science Editors for proofreading the manuscript, Jay Humphrey and Valentina Greco for critical reading. We thank Brian Coon for assistance during the preparation of the CRISR/Cas9 experiment. We thank Dr. Jun Lun's laboratory for providing miRNA reporter lentiviral plasmid. We thank Antonio Giraldez's laboratory for providing the zebrafish ago2 mutant. JS was funded by a Biotechnology and Biological Sciences Research Council (BBSRC) David Phillips Fellowship (BB/L024551/1). DMK was supported by F32HL132475, U54DK106857 and 1K99HL141687. VM was partially supported by a studentship from the Sir Richard Stapley Educational Trust. Mass spectrometry was carried out at the Wellcome Trust Centre for Cell-Matrix Research (WTCCMR; 203128/Z/16/Z) Proteomics Core Facility. This work was supported by USPHS grant RO1 GM47214 to MAS and RO1 HL130246 and AHA 17GRNT33460426 to SN.

References

1. Cyron CJ & Humphrey JD Growth and Remodeling of Load-Bearing Biological Soft Tissues. Meccanica 52, 645–664 (2017). [PubMed: 28286348]
2. Gilbert PM & Weaver VM Cellular adaptation to biomechanical stress across length scales in tissue homeostasis and disease. Semin Cell Dev Biol 67, 141–152 (2017). [PubMed: 27641825]
3. Humphrey JD, Dufresne ER & Schwartz MA Mechanotransduction and extracellular matrix homeostasis. Nat Rev Mol Cell Biol 15, 802–12 (2014). [PubMed: 25355505]
4. Humphrey JD Vascular adaptation and mechanical homeostasis at tissue, cellular, and sub-cellular levels. Cell Biochem Biophys 50, 53–78 (2008). [PubMed: 18209957]
5. Seki E & Brenner DA Recent advancement of molecular mechanisms of liver fibrosis. J Hepatobiliary Pancreat Sci 22, 512–8 (2015). [PubMed: 25869468]
6. Huang S & Ingber DE Cell tension, matrix mechanics, and cancer development. Cancer Cell 8, 175–6 (2005). [PubMed: 16169461]
7. Sun Z, Guo SS & Fassler R Integrin-mediated mechanotransduction. J Cell Biol 215, 445–456 (2016). [PubMed: 27872252]
8. Pasquinelli AE MicroRNAs and their targets: recognition, regulation and an emerging reciprocal relationship. Nat Rev Genet 13, 271–82 (2012). [PubMed: 22411466]
9. Hafner M et al. Transcriptome-wide identification of RNA-binding protein and microRNA target sites by PAR-CLIP. Cell 141, 129–41 (2010). [PubMed: 20371350]
10. Herranz H & Cohen SM MicroRNAs and gene regulatory networks: managing the impact of noise in biological systems. Genes Dev 24, 1339–44 (2010). [PubMed: 20595229]
11. Tsang J, Zhu J & van Oudenaarden A MicroRNA-mediated feedback and feedforward loops are recurrent network motifs in mammals. Mol Cell 26, 753–67 (2007). [PubMed: 17560377]
12. Kasper DM et al. MicroRNAs Establish Uniform Traits during the Architecture of Vertebrate Embryos. Dev Cell 40, 552–565 e5 (2017). [PubMed: 28350988]
13. Chi SW, Zang JB, Mele A & Darnell RB Argonaute HITS-CLIP decodes microRNA-mRNA interaction maps. Nature 460, 479–86 (2009). [PubMed: 19536157]
14. Byfield FJ, Reen RK, Shentu TP, Levitan I & Gooch KJ Endothelial actin and cell stiffness is modulated by substrate stiffness in 2D and 3D. J Biomech 42, 1114–9 (2009). [PubMed: 19356760]
15. Grimson A et al. MicroRNA targeting specificity in mammals: determinants beyond seed pairing. Mol Cell 27, 91–105 (2007). [PubMed: 17612493]
16. Saphirstein RJ & Morgan KG The contribution of vascular smooth muscle to aortic stiffness across length scales. Microcirculation 21, 201–7 (2014). [PubMed: 24635219]
17. Mullokandov G et al. High-throughput assessment of microRNA activity and function using microRNA sensor and decoy libraries. Nat Methods 9, 840–6 (2012). [PubMed: 22751203]
18. Kamata M, Liang M, Liu S, Nagaoka Y & Chen IS Live cell monitoring of hiPSC generation and differentiation using differential expression of endogenous microRNAs. PLoS One 5, e11834 (2010). [PubMed: 20676373]

19. Discher DE, Janmey P & Wang YL Tissue cells feel and respond to the stiffness of their substrate. Science 310, 1139–43 (2005). [PubMed: 16293750]
20. Kim YK, Kim B & Kim VN Re-evaluation of the roles of DROSHA, Export in 5, and DICER in microRNA biogenesis. Proc Natl Acad Sci U S A 113, E1881–9 (2016). [PubMed: 26976605]
21. Dupont S et al. Role of YAP/TAZ in mechanotransduction. Nature 474, 179–83 (2011). [PubMed: 21654799]
22. Kumar A et al. Talin tension sensor reveals novel features of focal adhesion force transmission and mechanosensitivity. J Cell Biol 213, 371–83 (2016). [PubMed: 27161398]
23. Bassett AR et al. Understanding functional miRNA-target interactions in vivo by site-specific genome engineering. Nat Commun 5, 4640 (2014). [PubMed: 25135198]
24. Shi-Wen X, Leask A & Abraham D Regulation and function of connective tissue growth factor/CCN2 in tissue repair, scarring and fibrosis. Cytokine Growth Factor Rev 19, 133–44 (2008). [PubMed: 18358427]
25. Kawakami A, Fukazawa T & Takeda H Early fin primordia of zebrafish larvae regenerate by a similar growth control mechanism with adult regeneration. Dev Dyn 231, 693–9 (2004). [PubMed: 15499559]
26. Mathew LK et al. Comparative expression profiling reveals an essential role for raldh2 in epimorphic regeneration. J Biol Chem 284, 33642–53 (2009). [PubMed: 19801676]
27. Mateus R et al. In vivo cell and tissue dynamics underlying zebrafish fin fold regeneration. PLoS One 7, e51766 (2012). [PubMed: 23284763]
28. Cifuentes D et al. A novel miRNA processing pathway independent of Dicer requires Argonaute2 catalytic activity. Science 328, 1694–8 (2010). [PubMed: 20448148]
29. Amelio I et al. miR-24 triggers epidermal differentiation by controlling actin adhesion and cell migration. J Cell Biol 199, 347–63 (2012). [PubMed: 23071155]
30. Nechiporuk A & Keating MT A proliferation gradient between proximal and msxb-expressing distal blastema directs zebrafish fin regeneration. Development 129, 2607–17 (2002). [PubMed: 12015289]
31. Hasegawa T et al. Transient inflammatory response mediated by interleukin-1beta is required for proper regeneration in zebrafish fin fold. Elife 6(2017).
32. Mateus R et al. Control of tissue growth by Yap relies on cell density and F-actin in zebrafish fin regeneration. Development 142, 2752–63 (2015). [PubMed: 26209644]
33. Mori M et al. Hippo signaling regulates microprocessor and links cell-density-dependent miRNA biogenesis to cancer. Cell 156, 893–906 (2014). [PubMed: 24581491]
34. Chaulk SG, Lattanzi VJ, Hiemer SE, Fahlman RP & Varelas X The Hippo pathway effectors TAZ/YAP regulate dicer expression and microRNA biogenesis through Let-7. J Biol Chem 289, 1886–91 (2014). [PubMed: 24324261]
35. Davis BN, Hilyard AC, Lagna G & Hata A SMAD proteins control DROSHA-mediated microRNA maturation. Nature 454, 56–61 (2008). [PubMed: 18548003]
36. Felix MA & Wagner A Robustness and evolution: concepts, insights and challenges from a developmental model system. Heredity (Edinb) 100, 132–40 (2008). [PubMed: 17167519]
37. Mouw JK et al. Tissue mechanics modulate microRNA-dependent PTEN expression to regulate malignant progression. Nat Med 20, 360–7 (2014). [PubMed: 24633304]
38. Liu G et al. miR-21 mediates fibrogenic activation of pulmonary fibroblasts and lung fibrosis. J Exp Med 207, 1589–97 (2010). [PubMed: 20643828]
39. Cushing L et al. miR-29 is a major regulator of genes associated with pulmonary fibrosis. Am J Respir Cell Mol Biol 45, 287–94 (2011). [PubMed: 20971881]
40. Herrera J et al. Dicer1 Deficiency in the IPF Fibroblastic Focus Promotes Fibrosis by Suppressing MicroRNA Biogenesis. Am J Respir Crit Care Med (2018).
41. Parker MW et al. Fibrotic extracellular matrix activates a profibrotic positive feedback loop. J Clin Invest 124, 1622–35 (2014). [PubMed: 24590289]
42. Pandit KV & Milosevic J MicroRNA regulatory networks in idiopathic pulmonary fibrosis. Biochem Cell Biol 93, 129–37 (2015). [PubMed: 25557625]

43. Wynn TA & Ramalingam TR Mechanisms of fibrosis: therapeutic translation for fibrotic disease. Nat Med 18, 1028–1040 (2012). [PubMed: 22772564]
44. Liu J et al. Argonaute2 is the catalytic engine of mammalian RNAi. Science 305, 1437–41 (2004). [PubMed: 15284456]
45. McCall MN et al. MicroRNA profiling of diverse endothelial cell types. BMC Med Genomics 4, 78 (2011). [PubMed: 22047531]
46. Krzywinski M et al. Circos: an information aesthetic for comparative genomics. Genome Res 19, 1639–45 (2009). [PubMed: 19541911]
47. Chi SW, Zang JB, Mele A & Darnell RB Argonaute HITS-CLIP decodes microRNA-mRNA interaction maps. Nature 460, 479–86 (2009). [PubMed: 19536157]
48. Dobin A et al. STAR: ultrafast universal RNA-seq aligner. Bioinformatics 29, 15–21 (2013). [PubMed: 23104886]
49. Li H et al. The Sequence Alignment/Map format and SAMtools. Bioinformatics 25, 2078–9 (2009). [PubMed: 19505943]
50. Kozomara A & Griffiths-Jones S miRBase: annotating high confidence microRNAs using deep sequencing data. Nucleic Acids Res 42, D68–73 (2014). [PubMed: 24275495]
51. Agarwal V, Bell GW, Nam JW & Bartel DP Predicting effective microRNA target sites in mammalian mRNAs. Elife 4(2015).
52. Aranguren XL et al. Unraveling a novel transcription factor code determining the human arterial-specific endothelial cell signature. Blood 122, 3982–92 (2013). [PubMed: 24108462]
53. Ritchie ME et al. limma powers differential expression analyses for RNA-sequencing and microarray studies. Nucleic Acids Res 43, e47 (2015). [PubMed: 25605792]
54. Bodenhofer U, Bonatesta E, Horejs-Kainrath C & Hochreiter S msa: an R package for multiple sequence alignment. Bioinformatics 31, 3997–9 (2015). [PubMed: 26315911]
55. Elosegui-Artola A et al. Mechanical regulation of a molecular clutch defines force transmission and transduction in response to matrix rigidity. Nat Cell Biol 18, 540–8 (2016). [PubMed: 27065098]
56. Kamata M, Liang M, Liu S, Nagaoka Y & Chen IS Live cell monitoring of hiPSC generation and differentiation using differential expression of endogenous microRNAs. PLoS One 5, e11834 (2010). [PubMed: 20676373]
57. Robinson MD, McCarthy DJ & Smyth GK edgeR: a Bioconductor package for differential expression analysis of digital gene expression data. Bioinformatics 26, 139–40 (2010). [PubMed: 19910308]
58. McCarthy DJ, Chen Y & Smyth GK Differential expression analysis of multifactor RNA-Seq experiments with respect to biological variation. Nucleic Acids Res 40, 4288–97 (2012). [PubMed: 22287627]
59. Goeminne LJ, Gevaert K & Clement L Peptide-level Robust Ridge Regression Improves Estimation, Sensitivity, and Specificity in Data-dependent Quantitative Label-free Shotgun Proteomics. Mol Cell Proteomics 15, 657–68 (2016). [PubMed: 26566788]
60. Tyanova S et al. The Perseus computational platform for comprehensive analysis of (prote)omics data. Nat Methods 13, 731–40 (2016). [PubMed: 27348712]
61. Smyth GK Linear models and empirical bayes methods for assessing differential expression in microarray experiments. Stat Appl Genet Mol Biol 3, Article3 (2004).
62. Berginski ME & Gomez SM The Focal Adhesion Analysis Server: a web tool for analyzing focal adhesion dynamics. F1000Res 2, 68 (2013). [PubMed: 24358855]
63. Gutierrez E & Groisman A Measurements of elastic moduli of silicone gel substrates with a microfluidic device. PLoS One 6, e25534 (2011). [PubMed: 21980487]
64. Han SJ, Oak Y, Groisman A & Danuser G Traction microscopy to identify force modulation in subresolution adhesions. Nat Methods 12, 653–6 (2015). [PubMed: 26030446]
65. Kapacee Z et al. Tension is required for fibripositor formation. Matrix Biol 27, 371–5 (2008). [PubMed: 18262777]
66. Cifuentes D et al. A novel miRNA processing pathway independent of Dicer requires Argonaute2 catalytic activity. Science 328, 1694–8 (2010). [PubMed: 20448148]

67. Narayanan A et al. In vivo mutagenesis of miRNA gene families using a scalable multiplexed CRISPR/Cas9 nuclease system. Sci Rep 6, 32386 (2016). [PubMed: 27572667]

68. Schindelin J et al. Fiji: an open-source platform for biological-image analysis. Nat Methods 9, 676–82 (2012). [PubMed: 22743772]

69. Le Guyader D et al. Origins and unconventional behavior of neutrophils in developing zebrafish. Blood 111, 132–41 (2008). [PubMed: 17875807]

70. Kasper DM et al. MicroRNAs Establish Uniform Traits during the Architecture of Vertebrate Embryos. Dev Cell 40, 552–565 e5 (2017). [PubMed: 28350988]

71. Sneddon IN The relation between load and penetration in the axisymmetric boussinesq problem for a punch of arbitrary profile. Int. J. Engng Sci. 3, 47–57 (1965).

72. Uren PJ et al. Site identification in high-throughput RNA-protein interaction data. Bioinformatics 28, 3013–20 (2012). [PubMed: 23024010]

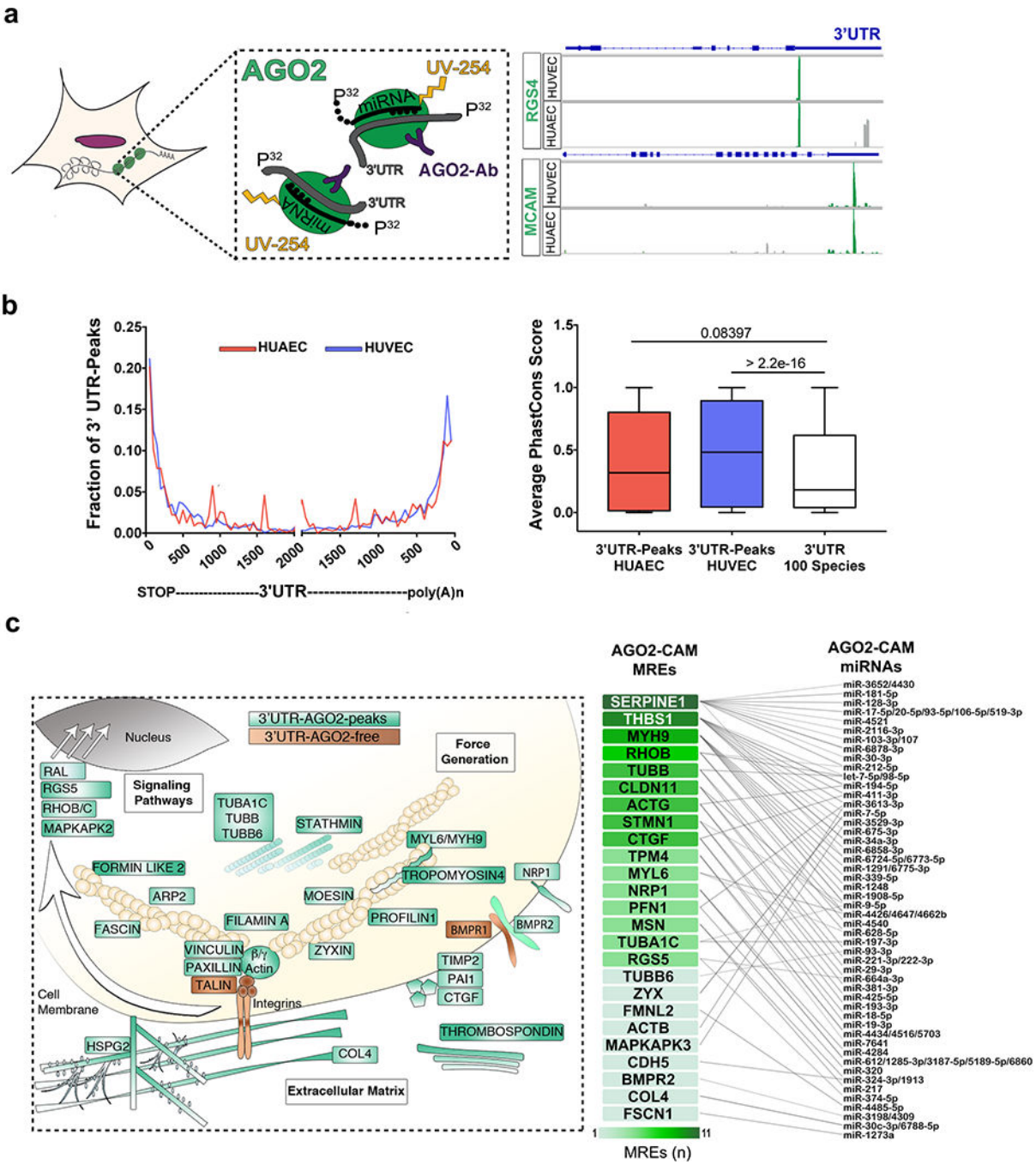

Figure 1. miRNAs regulate Cytoskeleton-Adhesion-Matrix (CAM) genes.

(a) Left, Schematic of AGO2-HITS-CLIP. miRNA-RNA complexes were cross-linked to AGO2 (green) via UV light and unbound RNAs removed by RNase treatment. AGO2-RNA complexes were immunoprecipitated, and RNA was labelled with 32-P and isolated. Right, an Integrative Genomics Viewer display of HITS-CLIP reads showed the sequences aligned within 30 to 70 nt intervals (AGO2 peak) within the 3'UTR region of the representative genes. Both HUAEC and HUVEC share the most significant peaks (green) **(b)** Left, chart represents positional enrichment of AGO2 peaks within the human 3'UTR for HUAEC (red)

and HUVEC (blue). Lines indicate the nt positional distribution of peak sequences within meta-gene analyzed 3'UTRs. Right chart shows difference in conservation scores across samples scoring using PhastCons (Wilcoxon Rank Sum Test). AGO2 peaks in HUAEC and HUVEC and binned human 3'UTRs were compared with binned 3'UTRs of 100 species. Conservation score is represented as a box plot with minimum, maximum, median and quartiles (n = 3 independent replica for HUVEC and HUAEC for a total of 383 for HUAEC, 749 for HUVEC and 125685 for Control individual value). **(c)** Left, Schematic shows cytoskeleton-adhesion-matrix (CAM) AGO2-regulome. AGO2-mRNA targets identified via AGO2-HIT-CLIP highlighted in green. Integrins, TALIN1 and BMPR1 proteins (brown) are part of CAM's GO term but were not detected by AGO2-HITS-CLIP. Arrows point to downstream regulators of CAM proteins targeted by AGO2. CAM proteins and their regulators were identified by database searches (Supplementary Fig. 1a, Supplementary tables 1–3) and manually curated for accuracy. Right chart shows interactome for 25 of the 73 AGO2-CAM genes in which a complementary MRE (7–8 nt) was identified using Target Scan v.7.0 prediction software and miRNAs were identified from AGO2-HITS-CLIP reads using miRbase (Methods). Color-coded boxes indicate the number of MREs identified in each of the selected CAM-gene 3'UTRs. Lines indicate interaction between MRE and miRNA family members with similar SEEDs. The mRNA-miRNA network shows high complexity, with numerous miRNAs binding one or more CAM-3'UTRs, while most CAM genes are targeted by more than one miRNA.

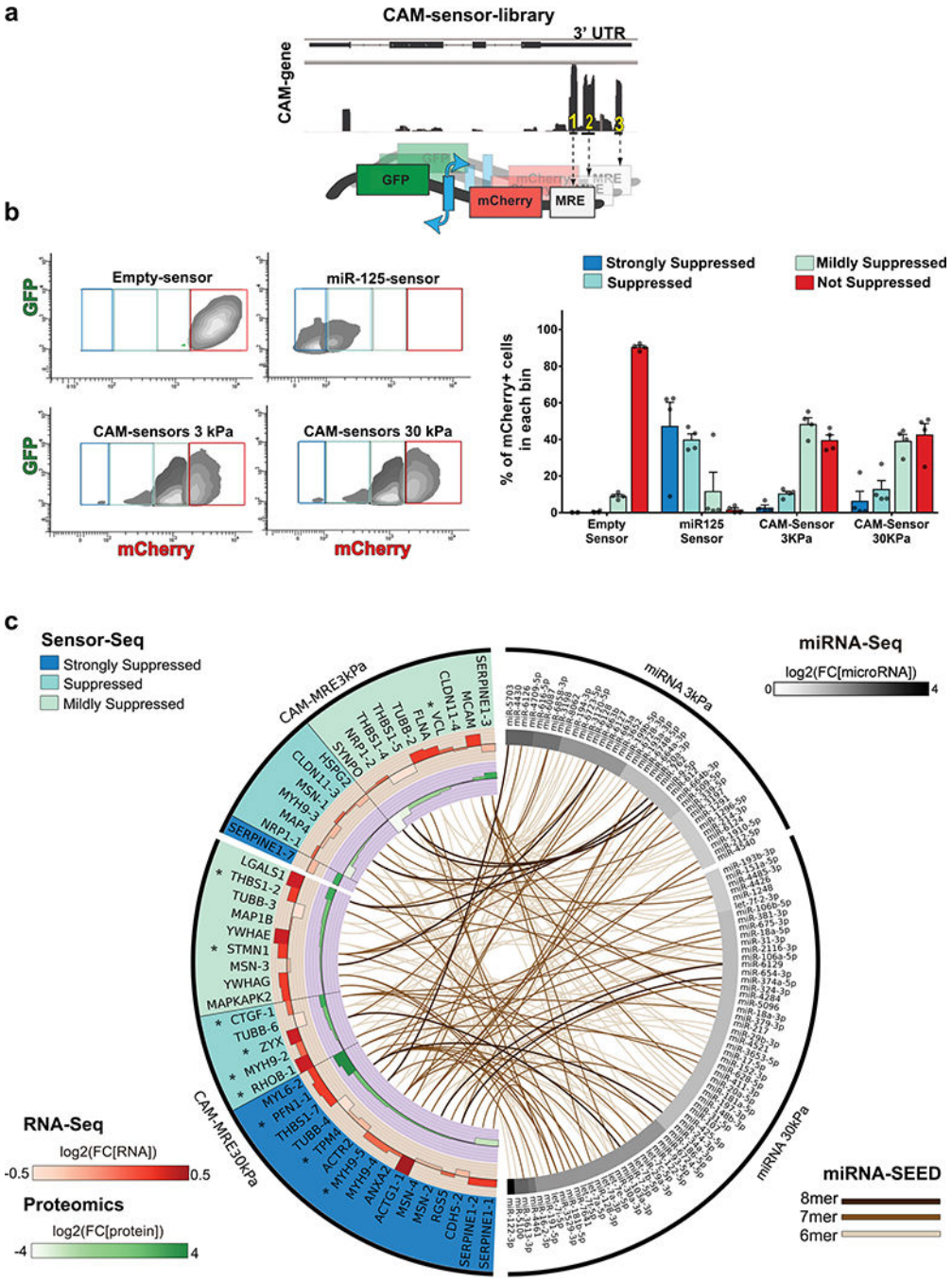

Figure 2. CAM-MREs are actively repressed in stiff substrates.

(a) Schematic for CAM sensor library. The Sensor-Seq lentiviral library (Methods) consisted of (1) mCherry upstream of one of the 97 CAM-MRE, and (2) GFP lacking any MRE (control). Numbered MREs indicate different MREs within one CAM 3'UTR, alternatively one MRE was cloned per CAM 3'UTR (Supplementary Table 4). **(b)** Left, mCherry and GFP intensities in HUVECs infected with the lentiviral library at 3 kPa and 30 kPa, a negative control (no MRE), and a positive control (3 perfect MREs for miR-125, abundant in HUVECs[45]). Density plots show relative intensity of cell distribution using contour lines.

Each contour line represents 15% of probability (higher= lighter grey, lower=darker grey) to contain cells in each bin over total cells (10,000 cells). Sensor-seq library-infected HUVECs at 3 kPa and 30 kPa were sorted into 4 bins, as indicated, based on mCherry/GFP expression relative to controls. Cells in each bin were isolated and genotyped using specific Illumina primer for sequencing (Methods). Right, Bar graph shows the percentage of mCherry+ cells sorted in each bin from 4 experiments (mean +/− SEM, single experiments are represented by dots) **(c)** CIRCOS[46] graphical representation of CAM miRNA-MRE interactions. Right quadrants: EC miRNAs with putative SEED matching to CAM MREs sensors displaying differential gene expression between 3 kPa and 30 kPa, divided in two groups: expressed at 3 kPa compared to 30 kPa (black line, top right) and expressed at 30 kPa compared to 3 kPa (black line, bottom right). Left quadrants: CAM-sensors most suppressed at 30 kPa compared to 3 kPa (black line, bottom left) and vice versa (black line, top left). Color-coded boxes indicate the categorized bins in (**b)** at which cells were isolated and genotyped for a specific CAM-Sensors. Lines indicate match between individual miRNA (SEED) and CAM MRE in each condition. Color code indicates the level of complementarity between miRNA SEED and MRE nucleotides. The internal circles show the respective CAM-RNAs (red) and proteins (green) log2 fold change at 3 kPa compared to 30 kPa and 30 kPa compared to 3 kPa (Supplementary tables 5–6). Source data can be found in Supplemental Table 8.

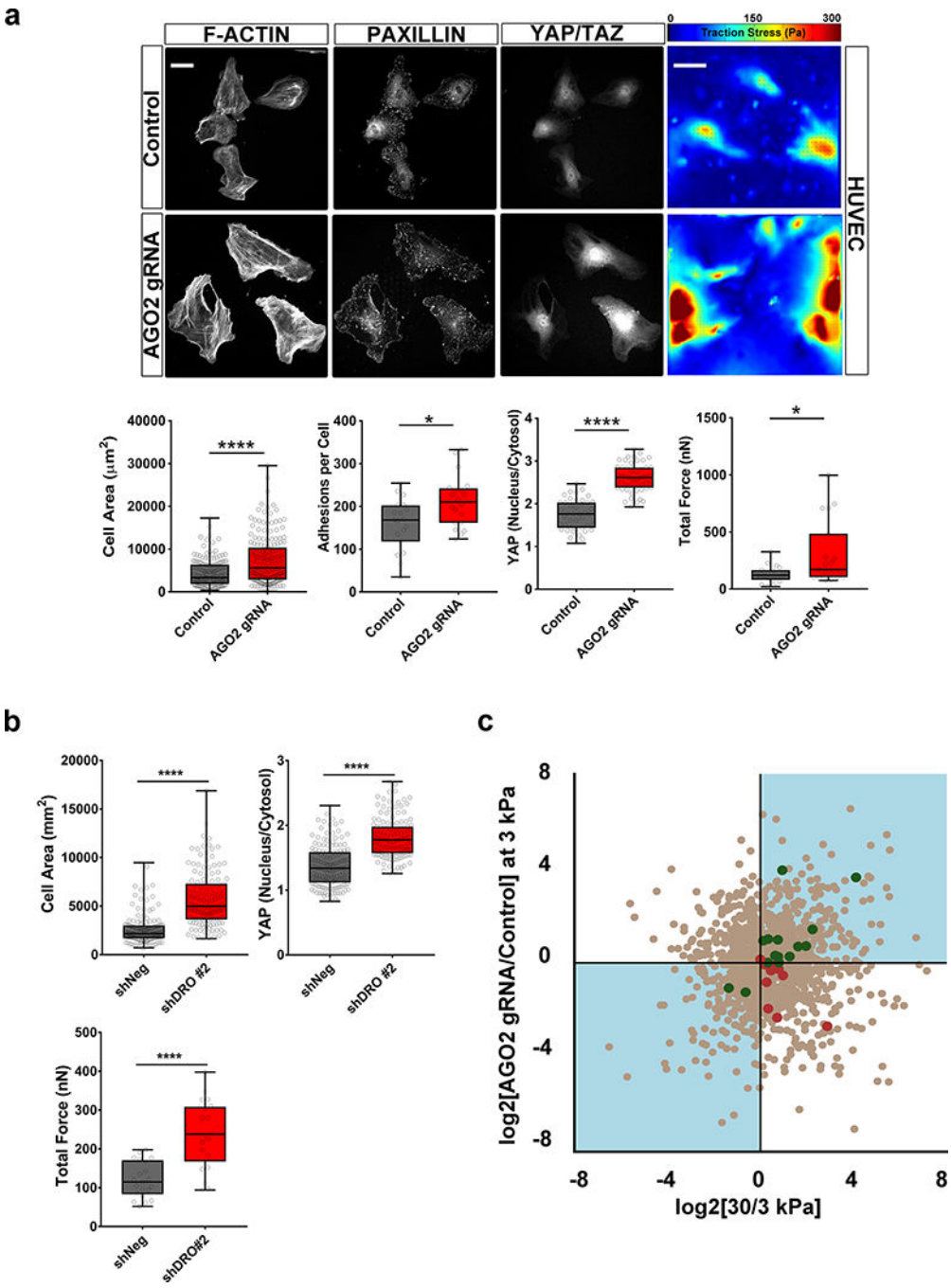

Figure 3. miRNAs limit ECs spreading, YAP signaling and contractility.

(a) Representative immunofluorescence images and traction force maps of HUVECs after infection with AGO2 or non-targeting control pLentiCRISPR virus. Cells on fibronectin-coated 3 kPa PDMS gels were stained for F-ACTIN (phalloidin), focal adhesions (PAXILLIN), and YAP/TAZ (scale bar = 50μm). Heat maps of traction stress for single cells (scale bar = 20μm). All box plots show the minimum, maximum, median and quartiles. Cell area (based on phalloidin staining) (Control n=163, AGO2gRNA n=182 cells/group, dots indicate individual cells, representative data from 6 independent experiments, ****

p<0.0001, unpaired two-sided t-test), number of PAXILLIN adhesions per cell (Control n=19 fields of view 49 cells, AGO2gRNA n=20 fields of view 51 cells, dots indicate average per field of view, representative data from 3 independent experiments, * p=0.0085, unpaired two-sided t-test), and nuclear to cytoplasmic ratio of YAP/TAZ (Control n=43 cells, AGO2gRNA n=54 cells, dots represent single cell measurements, representative data from 2 independent experiments, **** p<0.0001, unpaired two-sided t-test). Box plot for Total Force shows total force per single cell (n=19 cells / group, dots indicate individual cells, from two independent experiments, * p=0.0119, unpaired two-sided t-test). (**b**) Box plots show quantification of HUVEC treated with shRNA against DROSHA (methods) and seeded on fibronectin-coated 3kPa PDMS gels for cell spread area (shNeg n=156, shDRO#2 n=138 cells, from two independent experiments, **** p<0.0001, unpaired two-sided t-test), YAP nuclear localization (shNeg n=156, shDRO#2 n=138 cells, from two independent experiments, **** p<0.0001, unpaired two-sided t-test) and total force per cell (n=21 cells / group, from two independent experiments, **** p<0.0001, unpaired two-sided t-test). (**c**) Scatter plot representing difference in protein expression between HUVEC seeded on 30 vs. 3 kPa (x axis) or between HUVECs infected with AGO2 gRNA vs. control gRNA (y axis) (n=3 replicates). Green and red identify CAM proteins with coherent or incoherent differential expression, respectively (Supplementary Table 6). Source data can be found in Supplemental Table 8.

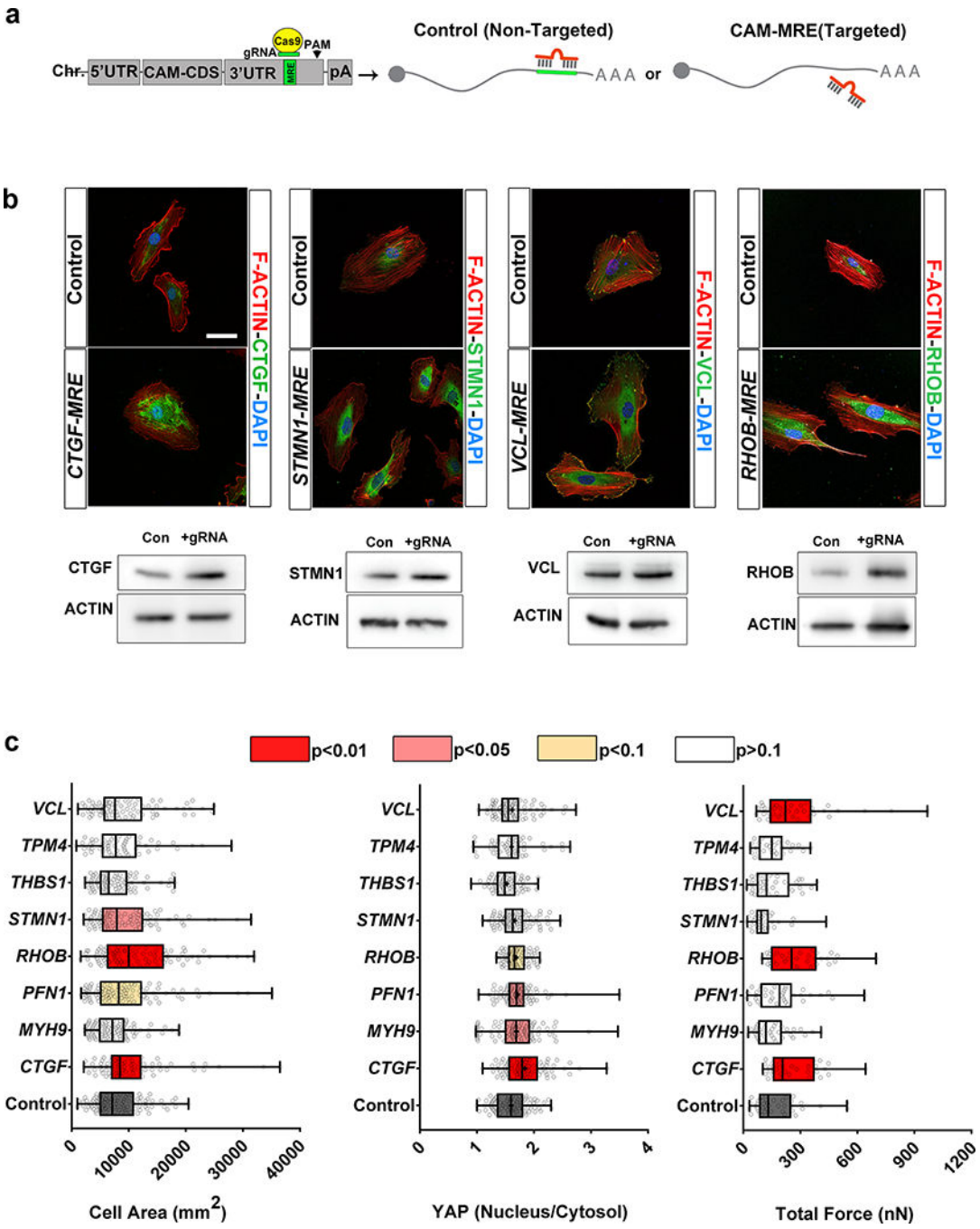

Figure 4. Post-transcriptional regulation of individual CAM genes limits ECs spreading, YAP signaling and/or contractility.

(**a**) Experimental strategy to mutate individual MREs in CAM genes' 3'UTRs to block miRNA binding (Methods and Supplementary Fig. 2b). (**b**) Representative immunofluorescence images (top, scale bar = 50μm) and Western blot (bottom) of CAM proteins as indicated (CTGF ~37 kDa, STMN1 ~19kDa, VCL ~116kDa, RHOB ~25kDa, Actin ~47kDa). HUVECs were infected with lentivirus carrying Cas9 and gRNA targeting specific CAM MREs and no-target gRNA (**a**) and processed at 7 days post infection. (**b**)

Quantification of cell spreading (n=99, 75, 91, 94, 88, 87, 79, 54, 83 from bottom to top, representative data from two independent experiments), YAP nuclear translocation (n=91, 81, 87, 93, 79, 88, 67, 54, 84 cells from bottom to top, representative data from two independent experiments) and total force per cell (n= 38, 33, 37, 36, 34, 34, 34, 30, 36 cells from bottom to top, from two independent experiments) in HUVECs on 3 kPa PDMS gels for 48 h after mutation of the indicated MREs (all box plots indicate the minimum, maximum, median and quartiles, single dots represent single cell, colors represent p values, one-way ANOVA with fishers LSD). Source data can be found in Supplemental Table 8.

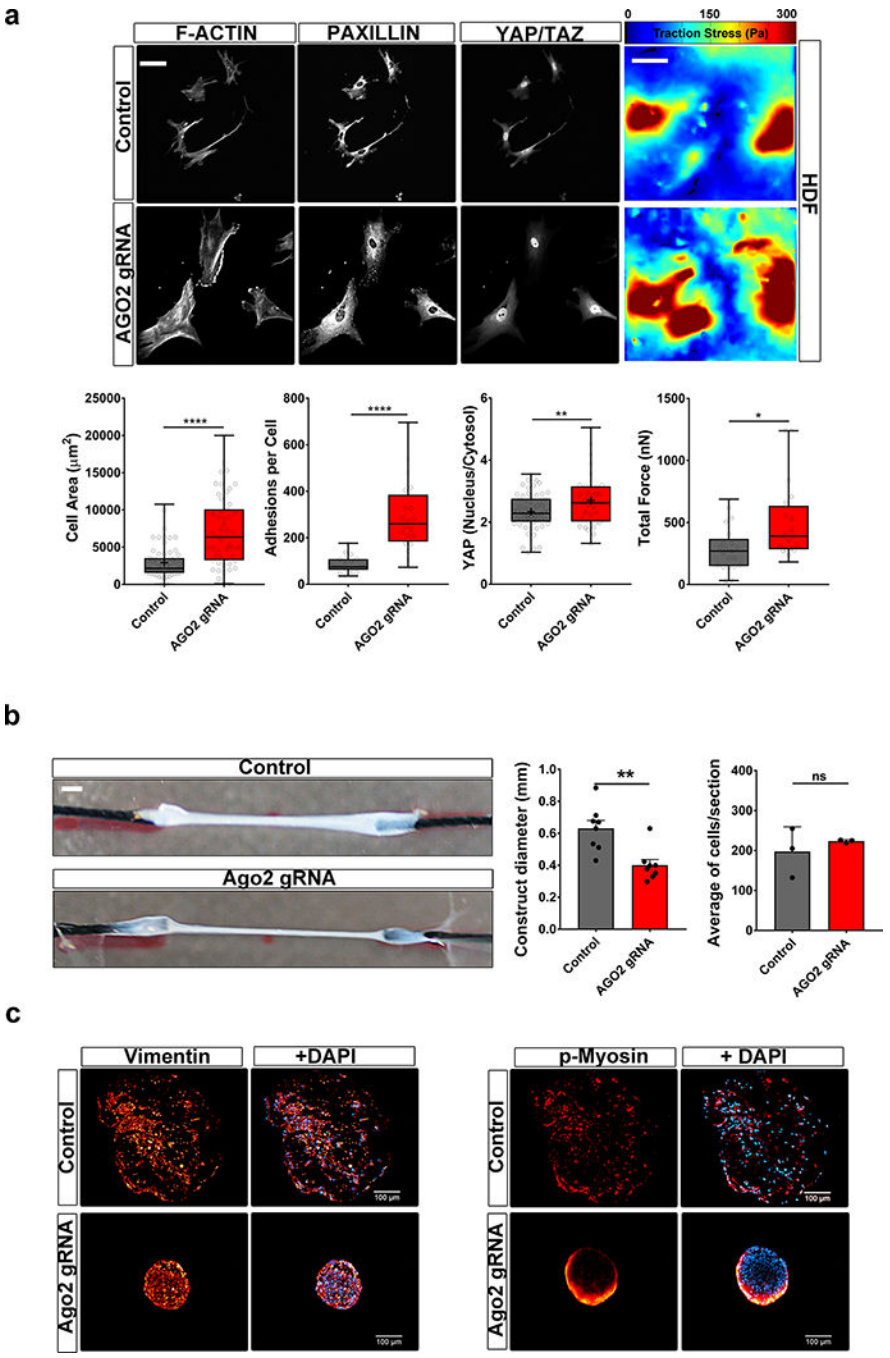

Figure 5. AGO2 activity is required to limit fibroblast contractility in 2- and 3-D models.

(a) Representative immunofluorescence images of HDF after infection with pLentiCRISPR virus directed at *AGO2* or a non-targeting control seeded on fibronectin coated 3 kPa PDMS gels for 48 hrs (scale bar = 50μm). Heat maps of traction stress for single cells (scale bar = 20μm). Box plots show HDF cell area (Control n = 63 cells, AGO2gRNA n=51 cells, representative data from 4 independent experiments, **** $p<0.001$, unpaired two-sided t-test) based on phalloidin staining, number of PAXILLIN adhesions per cell (n=19 fields of view 63 cells, AGO2 n=20 fields of view 51 cells, dots indicate average per field of view,

representative data from two independent experiments, **** p<0.0001, unpaired two-sided t-test), and nuclear to cytoplasmic ratio of YAP/TAZ (Control n=58 cells, AGO2gRNA n=34, cells represented by single dots, representative data from 2 independent experiments, * p=0.0174, unpaired two-sided t-test). Single cell maps of traction stress and quantification of total force per cell (box plot with whiskers indicate min and max value, Control n=21 cells, AGO2gRNA n=20 cells, * p=0.0109, unpaired two-sided t-test). **(b)** Representative 3D matrix constructs with control or Ago2-mutated mouse dermal fibroblasts (scale bar = 1mm). Bar plots show the average of cell number and construct diameter within transverse sections (n=8, bars indicate mean +/− SEM and dots represent single replicate, ** p<0.01, ns= non-significant). **(c)** Transverse sections of control and Ago2 depleted matrix constructs stained for Vimentin or pMyosin and DAPI (scale bar = 100μm). Source data can be found in Supplemental Table 8.

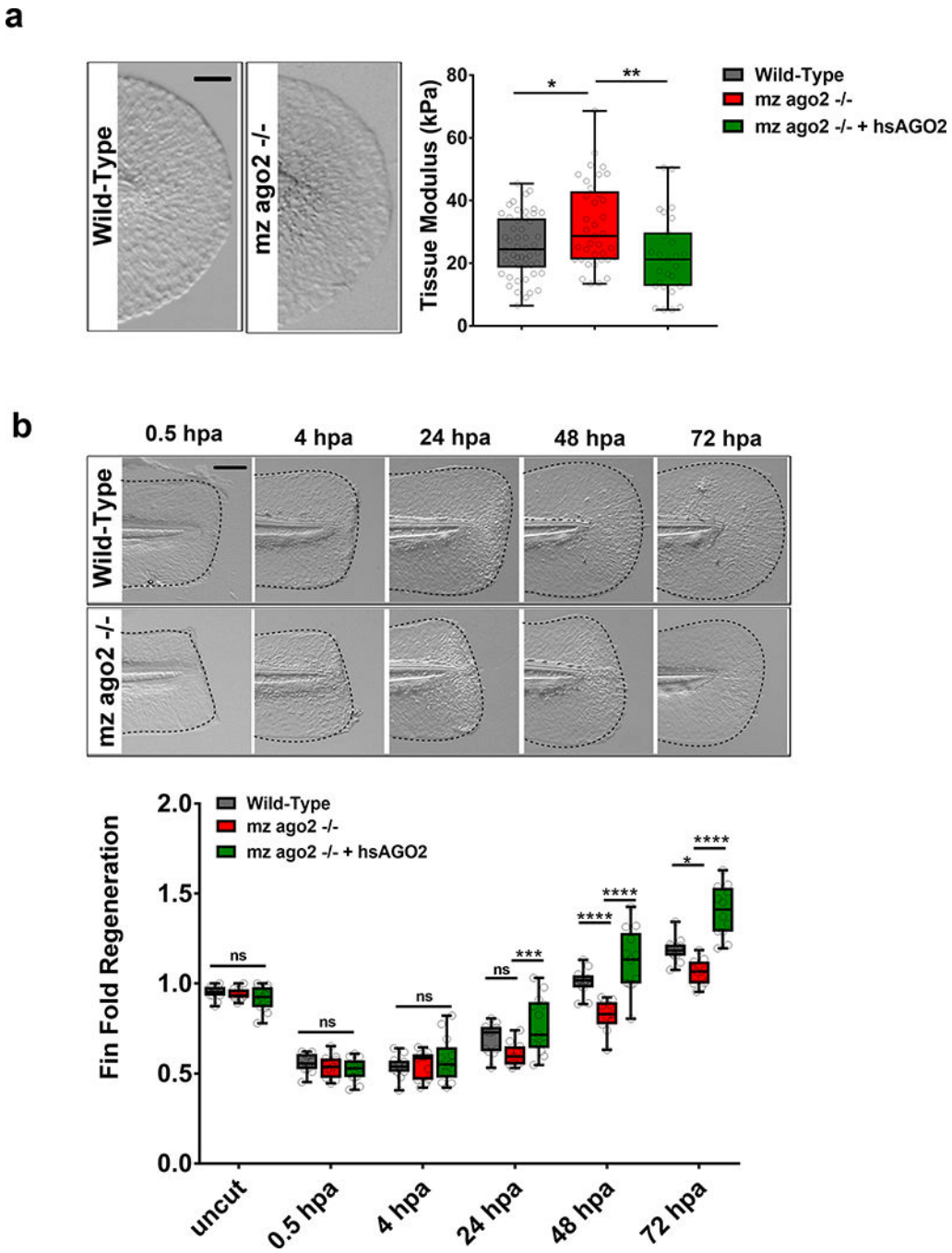

Figure 6. Ago2 activity is required for tissue stiffness and wound healing in the zebrafish fin-fold regeneration assay.

(**a**) Left, Bright field images of 48 hpf fin fold tissues in the indicated genotypes (scale bar = 0.05mm). Right, Elastic modulus of 48 hpf zebrafish fin fold surfaces of Wild-Type, *mz ago2 −/−* and *mz ago2 −/−* rescued with 200 pg of *in vitro* transcribed human Wild-Type AGO2 mRNA (*hs AGO2 mRNA)*. Embryos were harvested and adhered to a soft surface of PDMS in egg water. Elastic moduli were measured and AFM using NanoScope Analysis 1.5 software to fit force-deflection curves using the Sneadon model. At least two fin fold regions within each of 10–11 embryos were tested for each genotype (Wild-Type n=50, mz ago2−/−

n=37, mz ago2 −/− +hsAGO2 n=27 measurements; box plots indicate minimum, maximum, median and quartiles, single measures are represented by dots, combined data from 4 independent experiments, * p=0.0284, ** p=0.0033, One-way ANOVA with Tukey's multiple comparisons test). (**b**) Bright field images of zebrafish fin folds at the indicated stages and genotypes (head is to the left, scale bar = 0.1 mm). Dotted black line outlines the edge of the fin fold. Fin fold regeneration was assessed from the distance between the wound edge and the embryo body. One cell stage Wild-Type, *mz ago2−/−,* and *mz ago2−/−* embryos rescued with 200 pg of *hs AGO2 mRNA*. Values were normalized for the size of the fin-fold prior to injury (WT n=12, mz ago2 −/− n=11, mz ago2 −/− n=13, fish from 2 independent experiments, box plots indicate minimum, maximum, median and quartiles, dots indicate single fish measurements, *p=0.0168, ***p=0.0038; ****p<0.0001, two-way ANOVA with Sidak's multiple comparisons test). hpa= hours post amputation. Source data can be found in Supplemental Table 8.

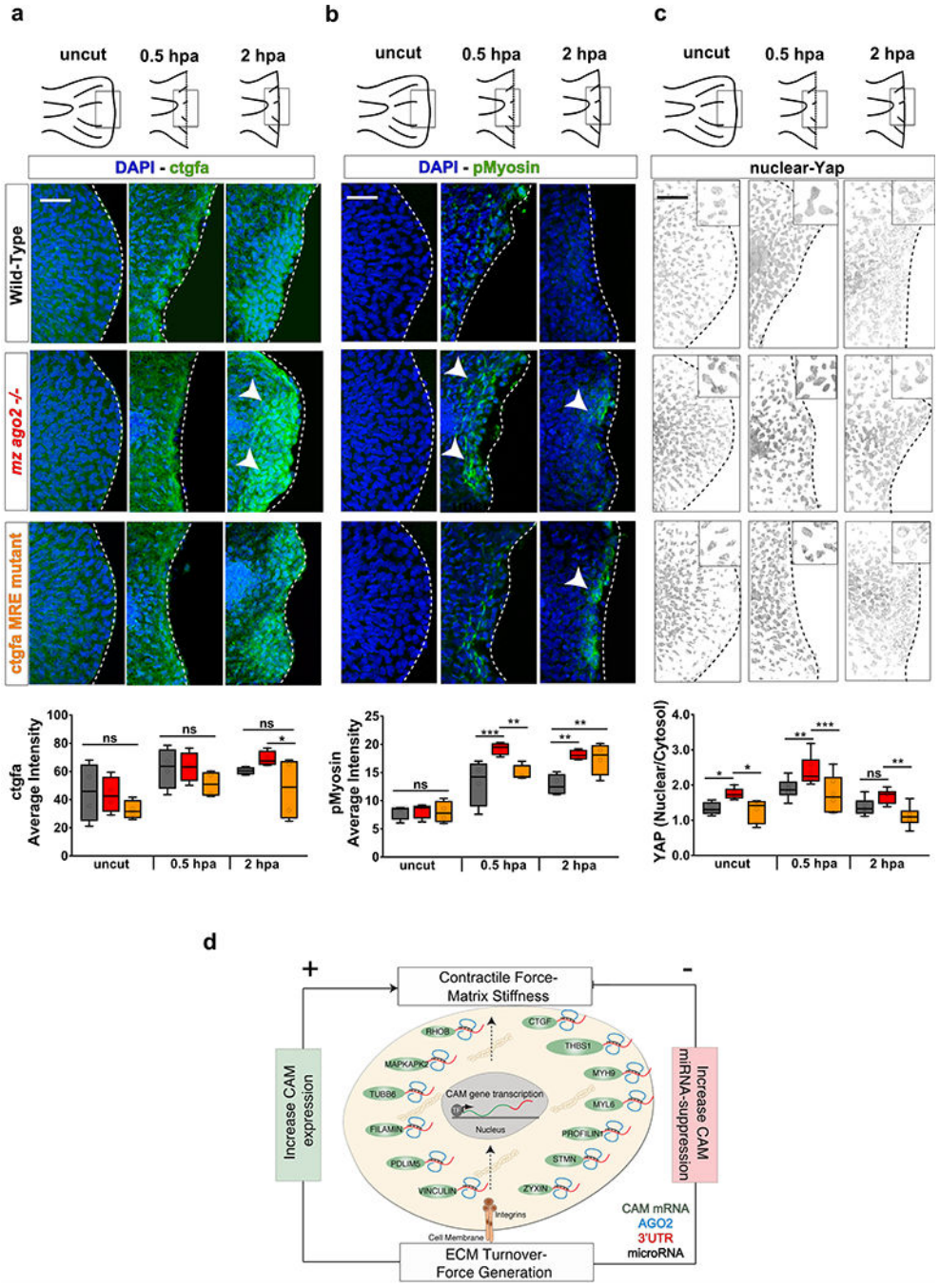

Figure 7. Wound healing in mz *ago2* and *ctgfa MRE* fin fold mutants.

(**a-c**) Top, schematics representing the time course of fin fold regeneration. Boxes identify the region of interest reported in the images below. Bottom, confocal images of whole mount fin folds within the boxed region from the cartoons at the top, at the indicated stages (scale bar = 120μm). White and black dotted lines indicate the edge of the fin fold. White arrowheads point to staining for the indicated markers. Graphs show box plot with minimum, maximum, median and quartiles. Intensity profiles for multiple embryos were combined (CTGF n=4 embryos per genotype, * in mz ago−/− 2h vs. ctgfaMRE mur 2h =

0.0318; pMyosin n=4 embryos per genotype, *** in WT 0h vs. mz ago−/− 0h = 0.0004, ** in mz ago−/− 0h vs. ctgfaMRE 0h = 0.0069, ** in WT 2h vs. mz ago−/− 2h = 0.0014, ** in WT 2h vs. ctgfaMRE 2h = 0.0041; YAP n=6 embryos for each genotype, * in WT uncut vs. mz ago−/− uncut = 0.027, * in ago uncut vs. ctgfaMRE uncut = 0.0126, ** in WT 0h vs. mz ago−/− 0h = 0.0082, *** in mz ago−/− 0h vs. ctgfa MRE 0h = 0.0008, ** in ago 2h vs. ctgf 2h = 0.0035; single fish represented by dots, n.s.= non-significant, unpaired two-sided t-test). For Yap the protein nuclear localization was represented. The nucleus/cytosol ration was obtained using the DAPI channel to generate a binary mask and subtract nuclear YAP-GFP intensity from the total YAP-GFP detected (Methods and Supplementary Fig. 7b). (**d**) Model for miRNA-post-transcriptional regulation of structural proteins function in mechanical tissue homeostasis. Increases in matrix stiffness and the resulting cell contractility increase integrin and actomyosin-dependent CAM signaling, which upregulates miRNAs that suppress CAM transcripts, thus restoring normal cell mechanics. Source data can be found in Supplemental Table 8.